

Microfluidization of Graphite and Formulation of Graphene-Based Conductive Inks

Panagiotis G. Karagiannidis,[†] Stephen A. Hodge,[†] Lucia Lombardi,[†] Flavia Tomarchio,[†] Nicolas Decorde,[†] Silvia Milana,[†] Ilya Goykhman,[†] Yang Su,[‡] Steven V. Mesite,[‡] Duncan N. Johnstone,[¶] Rowan K. Leary,[¶] Paul A. Midgley,[¶] Nicola M. Pugno,[§] Felice Torrisi,[†] and Andrea C. Ferrari^{*,†}

Cambridge Graphene Centre, University of Cambridge, Cambridge CB3 0FA, UK, Microfluidics International Corporation, Westwood, MA 02090, USA, Department of Materials Science and Metallurgy, University of Cambridge, Cambridge CB3 0FS, UK, and Department of Civil, Environmental and Mechanical Engineering, University of Trento, 38123 Trento, Italy
Center for Materials and Microsystems, Fondazione Bruno Kessler, 38123 Povo, TN, Italy
School of Engineering and Materials Science, Queen Mary University, London E1 4NS, UK

E-mail: acf26@eng.cam.ac.uk

KEYWORDS: graphene, solution processing, flexible electronics, conducting inks

Abstract

We report the exfoliation of graphite in aqueous solutions under high shear rate [$\sim 10^8 \text{ s}^{-1}$] turbulent flow conditions, with a 100% exfoliation yield. The material is stabilized without

*To whom correspondence should be addressed

[†]Cambridge Graphene Centre, University of Cambridge, Cambridge CB3 0FA, UK

[‡]Microfluidics International Corporation, Westwood, MA 02090, USA

[¶]Department of Materials Science and Metallurgy, University of Cambridge, Cambridge CB3 0FS, UK

[§]Department of Civil, Environmental and Mechanical Engineering, University of Trento, 38123 Trento, Italy
Center for Materials and Microsystems, Fondazione Bruno Kessler, 38123 Povo, TN, Italy
School of Engineering and Materials Science, Queen Mary University, London E1 4NS, UK

1
2
3 centrifugation at concentrations up to 100 g/L using carboxymethylcellulose sodium salt to
4 formulate conductive printable inks. The sheet resistance of blade coated films is below~
5 $2\Omega/\square$. This is a simple and scalable production route for conductive inks for large area printing
6
7 in flexible electronics.
8
9

10
11 Printed electronics combines conducting, semiconducting and insulating materials with printing
12 techniques, such as inkjet,¹ flexography,² gravure³ and screen.⁴ Metal inks based on Ag,⁵ Cu⁶
13 or Au,⁷ are used due to their high conductivity $\sigma \sim 10^7\text{S/m}$,^{5,8,9} making them the dominant tech-
14 nology in high frequency electronics (radio-frequency identification, RFID).^{10,11} For flexible elec-
15 tronic devices, *e.g.* organic photovoltaics (OPVs), a sheet resistance, $R_S [=1/\sigma h$, where h is the film
16 thickness] $< 10\Omega/\square$ is required,¹² while for printed RFID antennas one needs a few Ω/\square .¹³ To min-
17 imize R_S and cover the underneath rough layers, such as printed poly(3,4-ethylenedioxythiophene)
18 polystyrene sulfonate (PEDOT:PSS),¹⁴ thick films (μm range) are deposited using screen print-
19 ing.^{1,14-16} This is a technique in which the ink is forced mechanically by a squeegee through the
20 open areas of a stencil supported on a mesh of synthetic fabric.¹⁷ The ink must have high viscosity
21 ($>500\text{mPas}$),^{18,19} because lower viscosity inks run through the mesh rather than dispensing out of
22 it.¹⁸ To achieve this viscosity, typical formulations contain a conductive filler, such as Ag parti-
23 cles,²⁰ and insulating additives,¹⁷ at a total concentration higher than $C=100\text{g/L}$.¹⁷ Of this, $>60\text{g/L}$
24 consist of the conductive filler needed to achieve high $\sigma \sim 10^7\text{S/m}$.^{20,21} In 2016, the average cost
25 of Ag was $\sim 550\text{\$/Kg}$,²² that of Au $\sim 40,000\text{\$/Kg}$,²² while Cu was cheaper at $\sim 4.7\text{\$/Kg}$.²³ Although
26 metal oxidation issues under ambient conditions have been addressed as indicated in Refs.,^{6,24}
27 metal electrodes can degrade the device performance, by chemically reacting with photoactive
28 layers (Cu²⁵) or by migrating into device layers (Cu,²⁶ Ag²⁷). It was also reported that they
29 might cause water toxicity,²⁸ cytotoxicity,²⁹ genotoxicity,³⁰ and deoxyribonucleic acid (DNA)
30 damage.³¹ The average cost of graphite in 2016 was $\sim 1\text{\$/Kg}$,³² however, carbon-based inks are not
31 typically used to print electrodes in OPVs or RFIDs, due to their low $\sigma \sim 2-4 \times 10^3\text{S/m}$,³³⁻³⁵ which
32 corresponds to a $R_S \sim 20$ to $10\Omega/\square$ for a $25\mu\text{m}$ film. Thus, there is a need for cheap, stable and
33 non-toxic conductive materials.
34
35
36
37
38
39
40
41
42
43
44
45
46
47
48
49
50
51
52
53
54
55
56
57
58
59
60

1
2
3
4
5
6
7
8
9
10
11
12
13
14
15
16
17
18
19
20
21
22
23
24
25
26
27
28
29
30
31
32
33
34
35
36
37
38
39
40
41
42
43
44
45
46
47
48
49
50
51
52
53
54
55
56
57
58
59
60

Graphene is a promising alternative conductive filler.³⁶ Graphite can be exfoliated *via* sonication using solvents^{37–42} or water/surfactant solutions.^{40,43} Dispersions of single layer graphene (SLG) flakes can be produced at concentrations $\sim 0.01\text{g/L}$ ³⁷ with a yield by weight $Y_W \sim 1\%$,³⁷ where Y_W is defined as the ratio between the weight of dispersed material and that of the starting graphite flakes.⁴⁴ Dispersions of few layer graphene (FLG) flakes ($<4\text{nm}$) can be achieved with $C \sim 0.1\text{g/L}$ ⁴⁵ in N-Methyl-2-pyrrolidone (NMP) and $\sim 0.2\text{ g/L}$ in water.⁴⁰ The low $Y_W \sim 1\text{-}2\%$ ^{40,45} for FLG prepared by bath sonication is due to the fact that a significant amount of graphite remains unexfoliated as the ultrasonic intensity (*i.e.* the energy transmitted per unit time and unit area⁴⁶) is not uniformly applied in the bath^{46,47} and depends on the design and location of the ultrasonic transducers.⁴⁷ In tip sonication, the ultrasound intensity decays exponentially with distance from the tip,⁴⁸ and is dissipated at distances as low as $\sim 1\text{cm}$.⁴⁸ Therefore, only a small volume near the tip is processed.⁴⁹ Refs. 50,51 reported $\sim 2\text{nm}$ thick flakes with lateral size up to $\sim 70 \times 70\text{nm}^2$ and $C \sim 0.2\text{ g/L}$ with $Y_W = 1\%$ by tip sonication. In order to formulate screen printing inks,⁵¹ the flakes C was increased from 0.2 g/L to 80 g/L *via* repetitive centrifugation (4 times) and re-dispersion (3 times) processes, resulting in an increased preparation time. Ref. 52 used a rotor-stator mixer to exfoliate graphite, reaching $C < 0.1\text{g/L}$ of FLGs with $Y_W < 2 \times 10^{-3}$. Y_W is low because in mixers, a high shear rate, $\dot{\gamma}$, (*i.e.* the velocity gradient in a flowing material⁵³) is localized in the rotor stator gap^{52,54} and is $\sim 2 \times 10^4 - 1 \times 10^5\text{s}^{-1}$, dropping by a factor ~ 100 outside it.⁵⁴ Ref. 55 reported the production of FLGs with number of layers $N < 5$ and $Y_W > 70\%$ through electrochemical expansion of graphite in lithium perchlorate/propylene carbonate. The process required 3 cycles of electrochemical charging followed by $> 10\text{h}$ of sonication and several washing steps (with hydrochloric acid/dimethylformamide, ammonia, water, isopropanol and tetrahydrofuran) to remove the salts. A method with less processing steps and high Y_W (ideally 100%) remains a challenge.

Microfluidization is a homogenization technique whereby high pressure (up to 207MPa)⁵⁶ is applied to a fluid, forcing it to pass through a microchannel (diameter, $d < 100\mu\text{m}$), as shown in Fig.1, and discussed in Methods. The key advantage over sonication and shear-mixing is that high $\dot{\gamma} > 10^6\text{s}^{-1}$ is applied to the whole fluid volume,^{57,58} not just locally. Microfluidization was

1
2
3 used for the production of polymer nanosuspensions,⁵⁶ in pharmaceutical applications to produce
4 liposome nanoparticles to be used in eye drops,⁵⁹ to produce aspirin nanoemulsions,⁶⁰ as well
5 as in food applications for oil-in-water nanoemulsions.⁶¹ Microfluidization was also used for the
6 de-agglomeration and dispersion of carbon nanotubes.⁶²
7
8
9

10
11 Here, we report the production of FLGs with $Y_W \sim 100\%$ by microfluidization. The dispersion
12 is stabilized at a C up to ~ 100 g/L using carboxymethylcellulose sodium salt (CMC) (C=10g/L).
13 4% of the resulting flakes are < 4 nm and 96% are in the 4 to 70nm thickness range. The stabilized
14 dispersion is used for blade coating and screen printing. R_S of blade coated films after thermal
15 annealing (300°C-40 min) reaches $2\Omega/\square$ at $25\ \mu\text{m}$ ($\sigma=2 \times 10^4 \text{S/m}$), suitable for electrodes in de-
16 vices such as OPVs,^{12,63} organic thin-film transistors (OTFTs)⁶⁴ or RFIDs.¹³ The inks are then
17 deposited on glass and paper substrates using blade coating and screen printing to demonstrate the
18 viability for these applications (OPVs, OTFTs, RFIDs).
19
20
21
22
23
24
25
26
27
28
29

30 Results and discussion

31
32 We use Timrex KS25 graphite flakes as starting material. These are selected because their size is
33 suitable for flow in microchannels $\sim 87\ \mu\text{m}$ wide (90% are $< 27.2\ \mu\text{m}$ ⁶⁵). Larger flakes would cause
34 blockages. The flakes are used in conjunction with sodium deoxycholate (SDC) (Aldrich). SDC
35 is first mixed in deionized (DI) water ($\sigma=5.5 \times 10^{-6}$), the flakes are then added and treated with a
36 Microfluidic processor with a Z-type geometry interaction chamber (M-110P, Microfluidics), Fig1.
37 Mixtures are processed at the maximum pressure for this system ($\sim 207\text{MPa}$), with varying process
38 cycles (1-100). The temperature, T [°C] increases from 20 to 55°C after the liquid passes through
39 the interaction chamber. A cooling system reduces it to $\sim 20^\circ\text{C}$. This is important, otherwise T will
40 keep increasing and the solvent will boil. Graphite/SDC mixtures with increasing graphite C (1-
41 100g/L) and 9g/L SDC in DI water are processed over multiple cycles (1, 5, 10, 20, 30, 50, 70,
42 100). One cycle is defined as a complete pass through the interaction chamber.
43
44
45
46
47
48
49
50
51
52
53
54
55

56 Scanning electron microscopy (SEM) (Fig.2a) is used to assess the lateral size of the starting
57
58
59
60

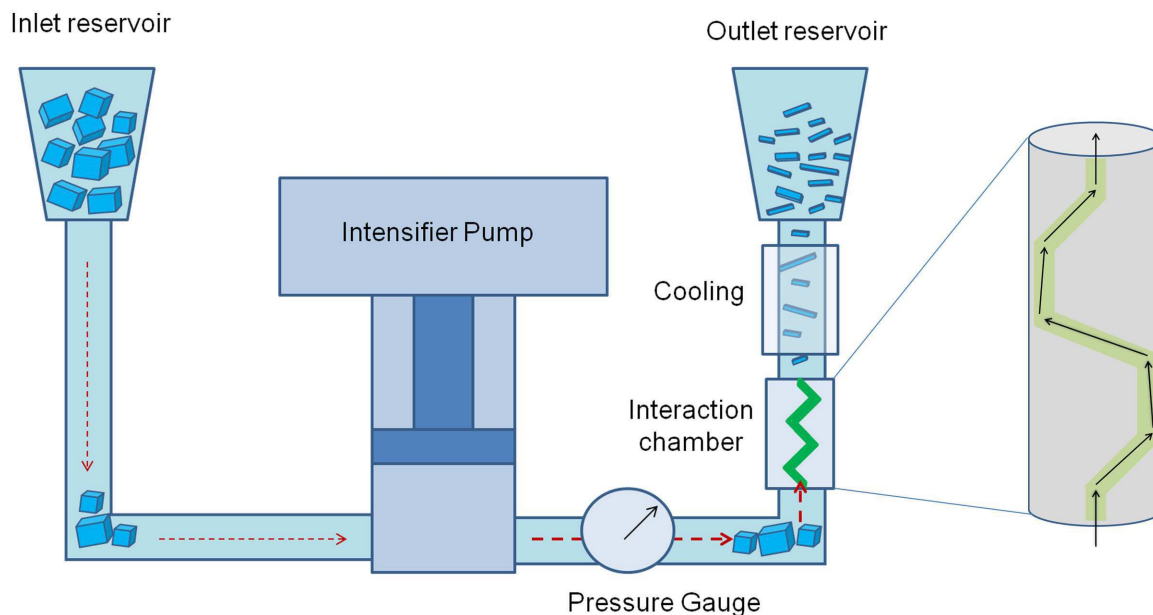


Figure 1: Schematic of the microfluidization process. Graphite flakes in SDC/water are added in the inlet reservoir. An intensifier pump applies high pressure (up to $\sim 207\text{MPa}$) and forces the suspension to pass through the microchannel of the interaction chamber where intense $\dot{\gamma} \sim 9.2 \times 10^7 \text{s}^{-1}$ is generated. The processed material is cooled and collected from the outlet reservoir. The process can be repeated several times.

flakes and of those exfoliated flakes after 5, 20 and 100 cycles. Dispersions are diluted (1000 times, from 50g/L to 0.05g/L) to avoid aggregation after they are drop cast onto Si/SiO_2 . The samples are further washed with five drops of a mixture of water and ethanol (50:50 in volume) to remove the surfactant. Three different magnifications are used. For each, images are taken at 10 positions across each sample. A statistical analysis of over 80 particles (Fig.2b) of the starting graphite reveals a lateral size (defined as the longest dimension) up to $\sim 32\mu\text{m}$. Following microfluidization, this reduces, accompanied by a narrowing of the flake distribution. After 100 cycles (Fig.2c), the mean flake size is $\sim 1\mu\text{m}$.

Atomic force microscopy (AFM) is performed after 20 and 100 cycles to determine h and aspect ratio ($\text{AR} = \text{lateral size}/h$). After 20 cycles, Fig.3(a,b) shows flakes with $d \sim 1.7\mu\text{m}$ and $h = 25\text{nm}$; $d = 1.9\mu\text{m}$ with $h = 8.5\text{nm}$, while Fig.3(c,d) shows $\sim 1\text{nm}$ flakes, consistent with N up to 3. AFM statistics of h and AR are also performed. Three samples, $\sim 60\mu\text{L}$, are collected from each dispersion (20 and 100 cycles) and drop cast onto $1\text{cm} \times 1\text{cm}$ Si/SiO_2 substrates. These are further

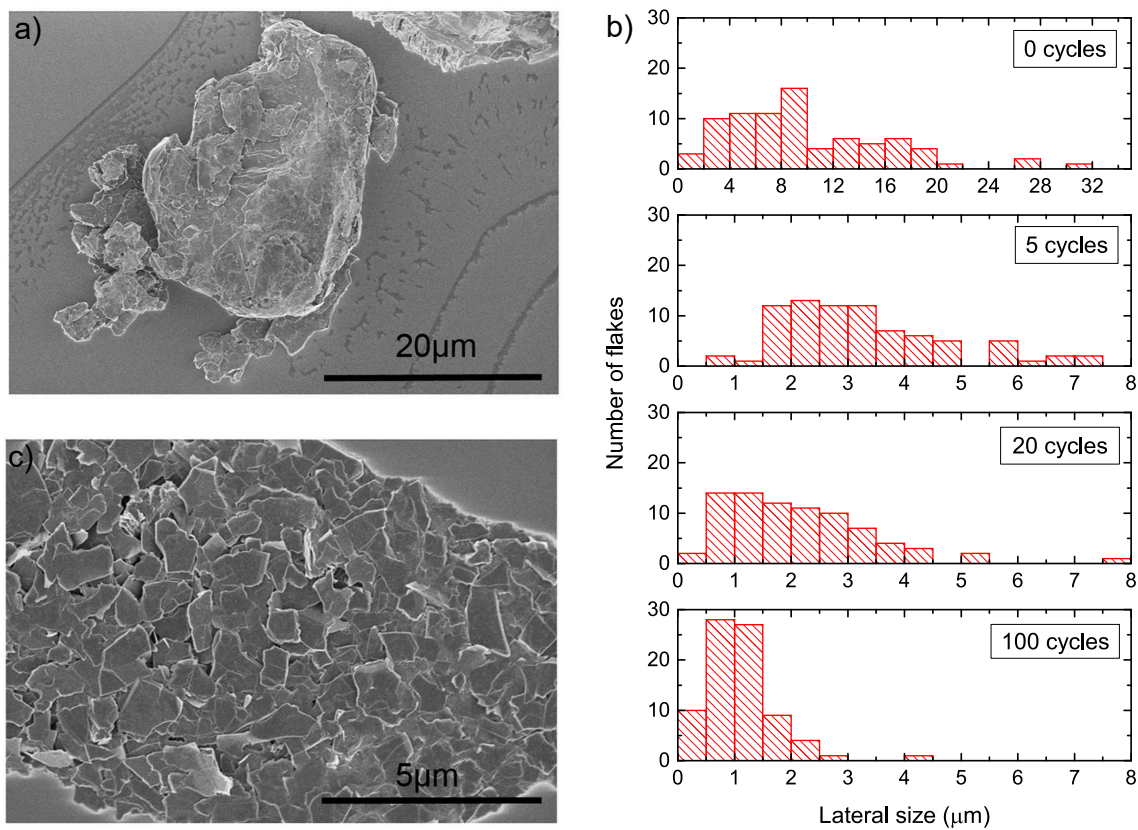


Figure 2: a) SEM image of pristine graphite flakes, b) histograms of lateral flake size for the starting material and after 5, 20 and 100 cycles, c) SEM image after 100 cycles.

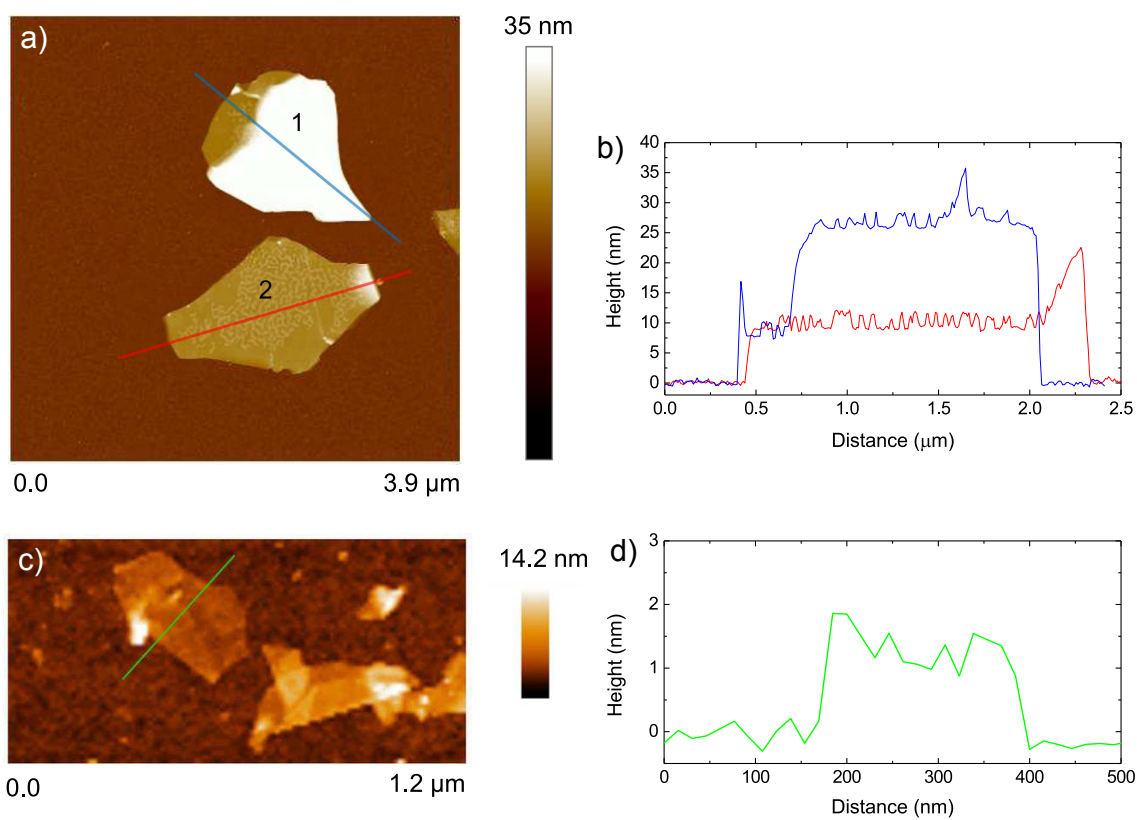
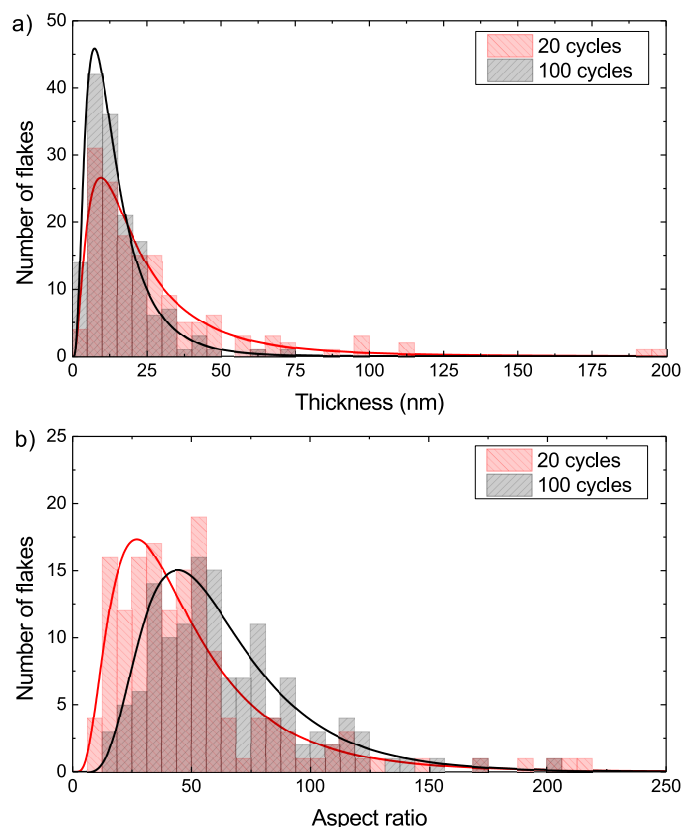


Figure 3: AFM images of typical flakes produced after 20 cycles: a) flakes with $h=8.5$ and 25nm . b) corresponding cross section profiles. c) flakes with $h=1\text{nm}$ and d) corresponding cross section.

1
2
3
4 washed with five drops of a mixture of water and ethanol (50:50 in volume) to remove the surfac-
5
6 tant. AFM scans are performed at 5 different locations on the substrate with each scan spanning
7
8 an area $\sim 20\mu\text{m} \times 20\mu\text{m}$. For each processing condition we measured 150 flakes. After 20 cycles,
9
10 h shows a lognormal distribution⁶⁶ peaked at $\sim 10\text{nm}$ (Fig.4a), with a mean value $\sim 19\text{nm}$. After
11
12 100 cycles (Fig.4a) the distribution is shifted towards lower h, with a maximum at $\sim 7.4\text{nm}$, a mean
13
14 $h \sim 12\text{nm}$ (4% of the flakes are $< 4\text{nm}$ and 96% are between 4 and 70nm). Fig.4b shows that AR
15
16 increases with processing cycles from ~ 41 for 20 cycles to ~ 59 for 100.



46
47
48
49
50
51
52
53
54
55
56
57
58
59
60

Figure 4: a) Flake thickness distribution and b) AR after 20 and 100 cycles, as measured by AFM.

The crystalline structure of individual flakes is investigated after 100 cycles (no statistical difference was observed between samples of different processing cycles) using scanning electron diffraction (SED)⁶⁷ with a Philips CM300 field emission gun transmission electron microscope (FEGTEM) operated at 50kV with a NanoMegastar Digistar system.⁶⁸ This enables the simultaneous scan and acquisition of diffraction patterns with an external optical CCD (charge-coupled device)

1
2
3
4 camera imaging the phosphor viewing screen of the microscope. Using SED, small angle con-
5
6
7
8
9
10
11
12
13
14
15
16
17
18
19
20
21
22
23
24
25
26
27
28
29
30
31
32
33
34
35
36
37
38
39
40
41
42
43
44
45
46
47
48
49
50
51
52
53
54
55
56
57
58
59
60

camera imaging the phosphor viewing screen of the microscope. Using SED, small angle convergent beam electron diffraction patterns are acquired at every position as the electron beam is scanned over 10 flakes with a step size of 10.6nm. Local crystallographic variations are visualized by plotting the diffracted intensity in a selected sub-set of pixels in each diffraction pattern as a function of probe position to form so-called "virtual dark-field" images.^{67,69} Fig.5a,c,e,g. shows the virtual dark-field images corresponding to the diffraction patterns in Fig.5b,d,f,h respectively. These show regions contributing to the selected Bragg reflection and therefore indicate local variations in the crystal structure and orientation. Consistent with selected area electron diffraction (SAED), three broad classes of flakes are observed, comprising (a,b) single crystals; (c,d) polycrystals with a small (<5) number of orientations, and (e-h) many (>5) small crystals. This shows that there is heterogeneity between individual flakes and that after 100 cycles a significant fraction (~70%) are polycrystalline.

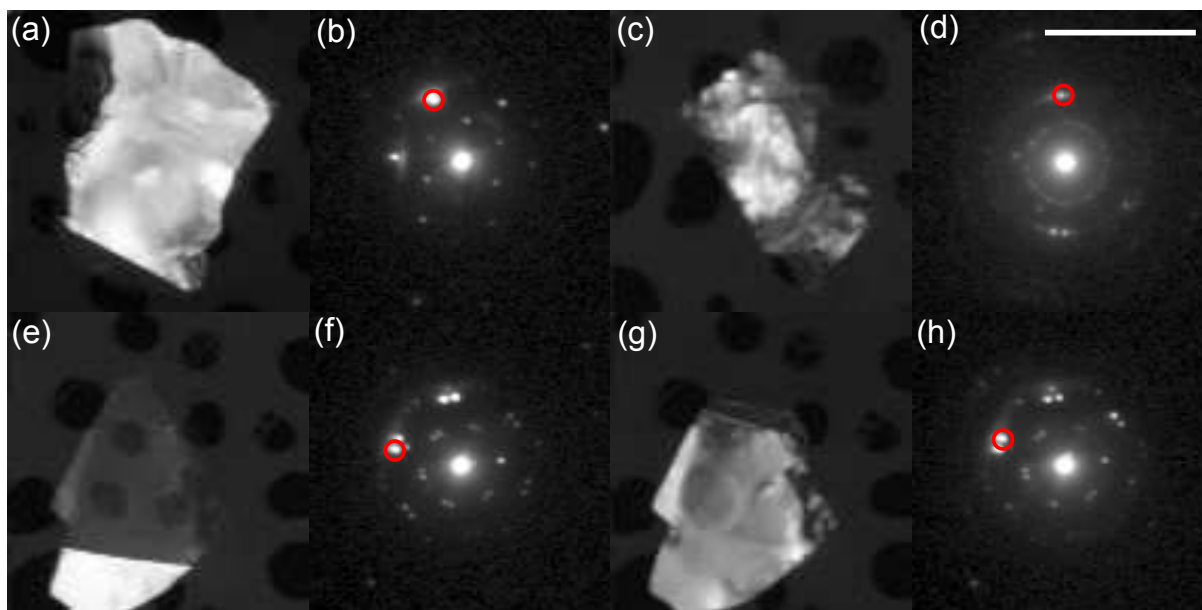


Figure 5: Virtual dark-field images (a,c,e,g) and representative diffraction patterns (b,d,f,h) acquired from (a,b) a single crystal flake, (c,d) a polycrystalline flake and (e-h) a polycrystalline flake comprising three crystals overlapping one another. The scale bar is 1 μ m.

It is important to assess any chemical changes, such as oxidation or other covalent functionalization that might occur during processing, since unwanted basal plane functionalisation may lead to a deterioration in electronic performance.⁷⁰ Flakes produced after 100 cycles are washed

1
2
3
4 by filtration to remove SDC prior to thermogravimetric analysis (TGA) and X-ray photoelectron
5 spectroscopy (XPS). For this washing procedure, 10mL isopropanol is added to 5mL dispersion
6 to precipitate the flakes. The resulting mixture is passed through a 70mm diameter filter and rinsed
7 with 500mL DI water followed by 500mL ethanol. The powder is dried under vacuum and scraped
8 from the filter paper. Inert atmosphere (nitrogen) TGA is performed to identify adsorbed or cova-
9 lently bonded functional groups using a TA Q50 (TA Instruments). Samples are heated from 25
10 to 100°C at 10°C/min, and then held isothermally at 100°C for 10 min to remove residual mois-
11 ture. T is then ramped to 1000°C at a typical heating rate of 10°C/min.⁷¹ The starting graphite
12 shows~2wt% decomposition above 700°C. Flakes after washing reveal no surfactant, as confirmed
13 by no weight loss at~400°C, where SDC suffers significant decomposition, as shown in Fig.6a.
14 However, thermal decomposition of the flakes occurs at~600°C, lower than the starting graphite,
15 with a weight loss~6wt%. Flakes with small lateral dimensions and thickness have a lower thermal
16 stability compared to large area graphitic sheets.^{73,74}

17
18
19
20
21
22
23
24
25
26
27
28
29
30
31 The starting graphite and the exfoliated flakes are then fixed onto adhesive Cu tape for XPS
32 (Escalab 250Xi, Thermo Scientific).⁷⁵ The binding energies are adjusted to the sp² C1s peak of
33 graphite at 284.5eV.⁷⁶⁻⁷⁸ Survey scan spectra (Fig.6b) of the starting graphite and the exfoliated
34 flakes reveal only C1s and O1s⁷⁶ peaks. The slight increase in oxygen content for the exfoliated
35 flakes compared to the starting material (C1s/O1s 35.1 to 25.9) is likely due to the increased ratio
36 of edge to basal plane sites as the flake lateral size decreases. However, C1s/O1s remains an order
37 of magnitude larger than the~3 typically observed in graphene oxide (GO).⁷⁹⁻⁸¹ Even following
38 reductive treatments, the C1s/O1s ratio in reduced graphene oxide (RGO) does not exceed~15,^{79,80}
39 *i.e.* half that measured for our flakes. High-energy resolution (50eV pass energy) scans are then
40 performed in order to deconvolute the C1s lineshapes. Both the starting graphite and exfoliated
41 flakes can be fitted with 3 components (Fig.6c-d): an asymmetric sp² C-C (284.5eV^{76,78}), C-O
42 (~285-286eV⁷⁸) and π - π^* transitions at~290eV.⁷⁸ Only a slight increase in the relative area of the
43 C-O peak is seen (from ~2% to ~5%). Therefore, we confirm that excessive oxidation or additional
44 unwanted chemical functionalisations do not occur during microfluidization.
45
46
47
48
49
50
51
52
53
54
55
56
57
58
59
60

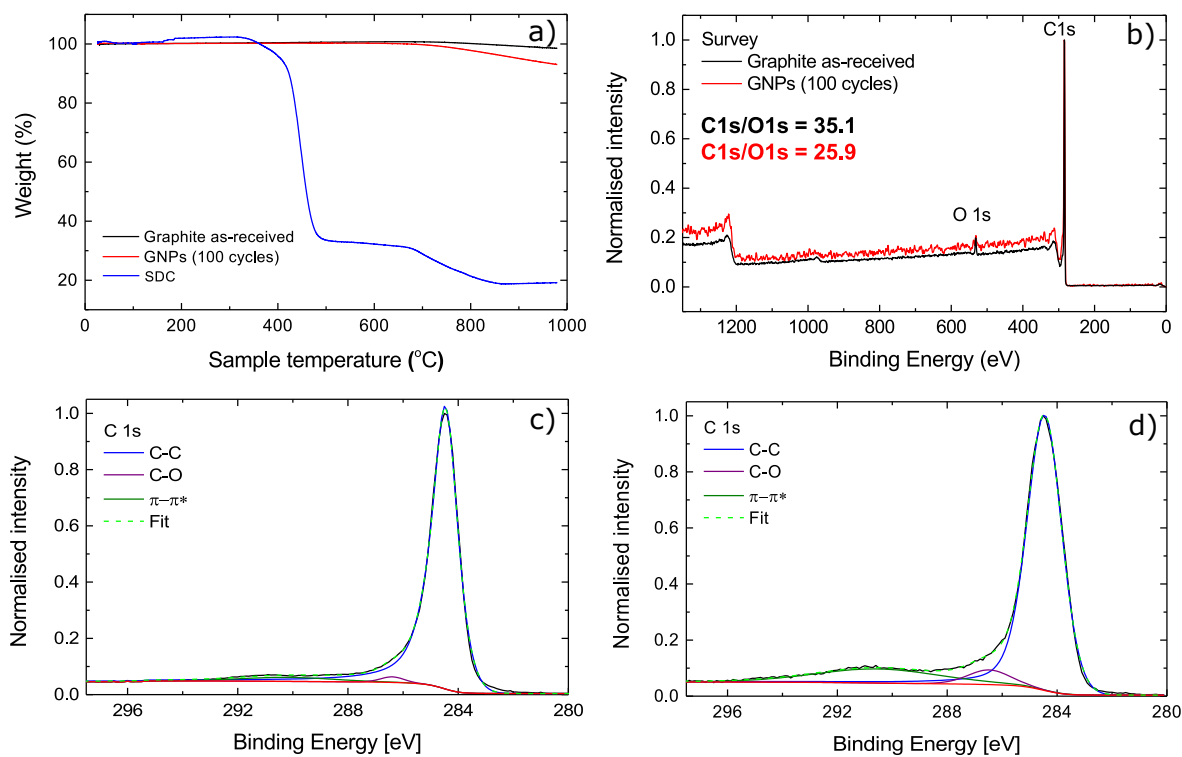


Figure 6: a) TGA of starting graphite, and flakes after 100 cycles and SDC in nitrogen. b) XPS of starting graphite and after 100 cycles. c-d) high-resolution C1s spectra of starting graphite and after 100 cycles. Red curves represent the Shirley-type⁷² background, which accounts for the effect of the inelastic scattering of electrons.

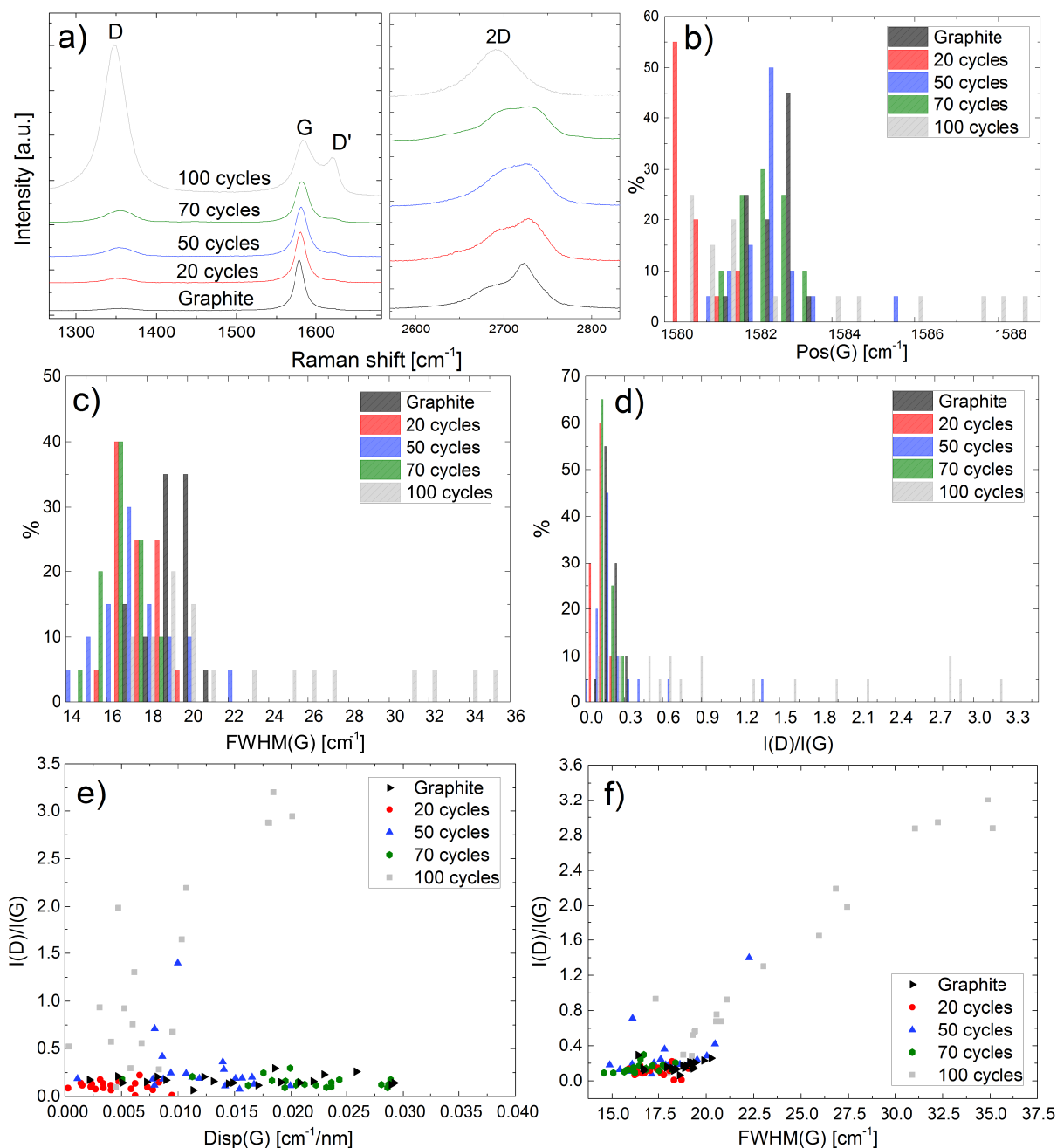


Figure 7: a) Representative Raman spectra at 514.5nm for graphite and after 20 (red curve), 50 (blue curve), 70 (green curve) and 100 (grey curve) cycles, b) Distribution of Pos(G), c) FWHM(G). e,f) I(D)/I(G) as a function of e) Disp(G) and f) FWHM(G).

1
2
3
4 Raman spectroscopy is then used to assess the structural quality of the flakes. $\sim 60\mu L$ of aque-
5
6 ous dispersion is drop cast onto 1cm x 1cm Si/SiO₂ substrates, then heated at 80-100 °C for 20
7
8 min, to ensure water evaporation, and washed with a mixture of water and ethanol (50:50 in vol-
9
10 ume) to remove SDC. Raman spectra are acquired at 457, 514 and 633 nm using a Renishaw InVia
11
12 spectrometer equipped with a 50x objective. The power on the sample is kept below 1mW to
13
14 avoid any possible damage. The spectral resolution is $\sim 1\text{cm}^{-1}$. A statistical analysis is performed
15
16 on the starting graphite and on samples processed for 20, 50, 70 and 100 cycles. The spectra are
17
18 collected by using a motorized stage as follows: the substrate is divided in nine equally spaced
19
20 regions $\sim 200 \times 200\mu\text{m}^2$. In each, 3 points are acquired. This procedure is repeated for for each sam-
21
22 ple and for the 3 wavelengths. The Raman spectrum of graphite has several characteristic peaks.
23
24 The G peak corresponds to the high frequency E_{2g} phonon at Γ .⁸² The D peak is due to the breath-
25
26 ing modes of six-atom rings and requires a defect for its activation.⁸³ It comes from transverse
27
28 optical (TO) phonons around the Brillouin zone corner K.^{82,83} It is active by double resonance
29
30 (DR)^{84,85} and is strongly dispersive with excitation energy⁸⁶ due to a Kohn Anomaly (KA) at K.⁸⁷
31
32 DR can also happen as an intravalley process, *i.e.* connecting two points belonging to the same
33
34 cone around K (or K'). This gives the so-called D' peak. The 2D peak is the D-peak overtone, and
35
36 the 2D' peak is the D' overtone. Because the 2D and 2D' peaks originate from a process where
37
38 momentum conservation is satisfied by two phonons with opposite wave vectors, no defects are
39
40 required for their activation, and are thus always present.⁸⁸⁻⁹⁰ The 2D peak is a single Lorentzian
41
42 in SLG, whereas it splits in several components as N increases, reflecting the evolution of the elec-
43
44 tronic band structure.⁸⁸ In bulk graphite it consists of two components, $\sim 1/4$ and $1/2$ the height of
45
46 the G peak.⁸⁸ In disordered carbons, the position of the G peak, Pos(G), increases with decreas-
47
48 ing of excitation wavelength (λ_L),⁹¹ resulting in a non-zero G peak dispersion, Disp(G), defined
49
50 as the rate of change of Pos(G) with excitation wavelength. Disp(G) increases with disorder.⁹¹
51
52 Analogously to Disp(G), the full width at half maximum of the G peak, FWHM(G), increases with
53
54 disorder.⁹² The analysis of the intensity ratio of the D to G peaks, I(D)/I(G), combined with that of
55
56 FWHM(G) and Disp(G), allows one to discriminate between disorder localized at the edges and in
57
58
59
60

1
2
3 the bulk. In the latter case, a higher $I(D)/I(G)$ would correspond to higher $FWHM(G)$ and $Disp(G)$.
4
5 Fig.7a plots representative spectra of the starting graphite (black line) and of flakes after 20 (red
6 line), 50 (blue line), 70 (green line) and 100 cycles (grey line). The 2D band lineshape for the
7 starting graphite and the 20-70 cycles samples shows two components ($2D_2, 2D_1$). Their intensity
8 ratio, $I(2D_2)/I(2D_1)$, changes from ~ 1.5 for starting graphite to ~ 1.2 for 50 and 70 cycles, until
9 the 2D peak becomes a single lorentzian for 100 cycles, suggesting an evolution to electronically
10 decoupled layers.^{90,93} $FWHM(2D)$ for 100 cycles is $\sim 70\text{cm}^{-1}$, significantly larger than in pristine
11 graphene. This implies that, even if the flakes are multilayers, they are electronically decoupled
12 and, to a first approximation, behave as a collection of single layers. $Pos(G)$ (Fig.7b), $FWHM(G)$
13 (Fig.7c) and $I(D)/I(G)$ (Fig.7d) for 20-70 cycles do not show a significant difference with respect
14 to the starting graphite. However, for 100 cycles, $Pos(G)$, $FWHM(G)$ and $I(D)/I(G)$ increase up
15 to ~ 1588 , 34cm^{-1} and 3.2, suggesting a more disordered material. For all the processed samples
16 (20-100) the D peak is present. For 20-70 cycles, it mostly arises from edges, as supported by
17 the absence of correlation between $I(D)/I(G)$, $Disp(G)$ (Fig.7e) and $FWHM(G)$ (Fig.7f). The cor-
18 relation between $I(D)/I(G)$, $Disp(G)$ (Fig.7e) and $FWHM(G)$ (Fig.7f) for 100 cycles indicates that
19 D peak arises not only from edges, but also from in-plane defects. Therefore, we select 70 cy-
20 cles to formulate conductive printable inks. We note that here we use synthetic microcrystalline
21 graphite flakes instead of large natural or single crystal flakes sometimes used by other LPE-based
22 papers.^{37,52,55,94,95} Our flakes produced up to 70 cycles are of comparable quality, as shown by
23 Raman spectroscopy.

24
25
26
27
28
29
30
31
32
33
34
35
36
37
38
39
40
41
42
43
44 **Printable inks formulation.** Following microfluidization, carboxymethylcellulose sodium salt
45 (CMC) (Weight Average Molecular Weight, $M_W = 700.000$, Aldrich No.419338), a biopolymer⁹⁶
46 which is a rheology modifier,^{97,98} is added to the dispersion to stabilize the flakes against sedi-
47 mentation. CMC is added at $C=10$ g/L over a period of 3h at room temperature. This is necessary
48 because if all CMC is added at once, aggregation occurs, and these aggregates are very difficult
49 to dissolve. The mixture is continuously stirred until complete dissolution. Different inks are pre-
50 pared, keeping constant the SDC $C=9$ g/L and CMC $C=10$ g/L, while increasing the flakes C to 1,
51
52
53
54
55
56
57
58
59
60

1
2
3 10, 20, 30, 50, 80, 100 g/L. Once printed and dried, these formulations correspond to 5, 35, 51, 61,
4
5 73, 81 and 84 wt% total solids content, respectively.
6

7
8 The rheological properties are investigated using a Discovery HR-1 rheometer (TA Instru-
9
10 ments) in a parallel-plate (40mm diameter) configuration.⁹⁹ We monitor the elastic modulus G'
11 [J/m³=Pa], representing the energy density stored by the material under shear,¹⁰⁰ and the loss
12 modulus G'' [J/m³=Pa],¹⁰⁰ representing the energy density lost during a shear process due to fric-
13
14 tion and internal motions.¹⁰⁰ Flow curves are measured by increasing $\dot{\gamma}$ from 1 to 1000s⁻¹ at a gap
15
16 of 0.5mm, because this $\dot{\gamma}$ range is applied during screen printing.¹⁰¹ Fig.8a plots the steady state
17
18 viscosity of an ink containing 73% wt flakes (100 cycles) as a function of $\dot{\gamma}$. CMC imparts a drop in
19
20 viscosity under shearing, from 570mPa.s at 100s⁻¹ to 140mPa.s at 1000s⁻¹. This is a thixotropic
21
22 behavior,¹⁰² since the viscosity reduces with $\dot{\gamma}$. The higher $\dot{\gamma}$, the lower the viscosity.¹⁰² This
23
24 behavior is shown by some non-Newtonian fluids, such as polymer solutions¹⁰³ and biological
25
26 fluids.¹⁰⁴ It is caused by the disentanglement of polymer coils or by the increased orientation of
27
28 polymer coils in the direction of the flow.¹⁰² On the other hand, in Newtonian liquids the viscosity
29
30 does not change with $\dot{\gamma}$.¹⁰⁴ Refs. 105,106 reported that thixotropy in CMC solutions arises from
31
32 the presence of unsubstituted (free) OH groups. Thixotropy decreases as the number of OH groups
33
34 increases.^{105,106}
35
36
37

38
39 During printing, shear is applied to the ink and its viscosity decreases, making the ink easier to
40
41 print or coat. This shear thinning behavior facilitates the use of the ink in techniques such as screen
42
43 printing, in which a maximum $\dot{\gamma} \sim 1000\text{s}^{-1}$ is reached when the ink penetrates the screen mesh.¹⁰¹
44
45 Fig.8b plots the viscosity at 100s⁻¹ as a function of wt% flakes (70 process cycles). This drops
46
47 from 0.56 to 0.43Pa.s with the addition of 5 wt% flakes, and recovers above 50 wt% flakes. The
48
49 CMC polymer (10 g/L in water) has $\mu \sim 0.56\text{Pa s}$ at 100s⁻¹, and drops to 0.43Pa s with the addition
50
51 of 5 wt% flakes. The flakes wt% affects $\dot{\gamma}$, which increases reaches 0.6Pa s at 80 wt%.

52
53 More information on the ink rheological behavior and microstructure can be obtained by os-
54
55 cillatory rheology measurements.¹⁰⁷ CMC gives a viscoelastic character to the ink. This can also
56
57 be evaluated in terms of the loss factor defined as $\tan\delta = G''/G'$.¹⁰⁰ The lower $\tan\delta$, the more solid-
58
59
60

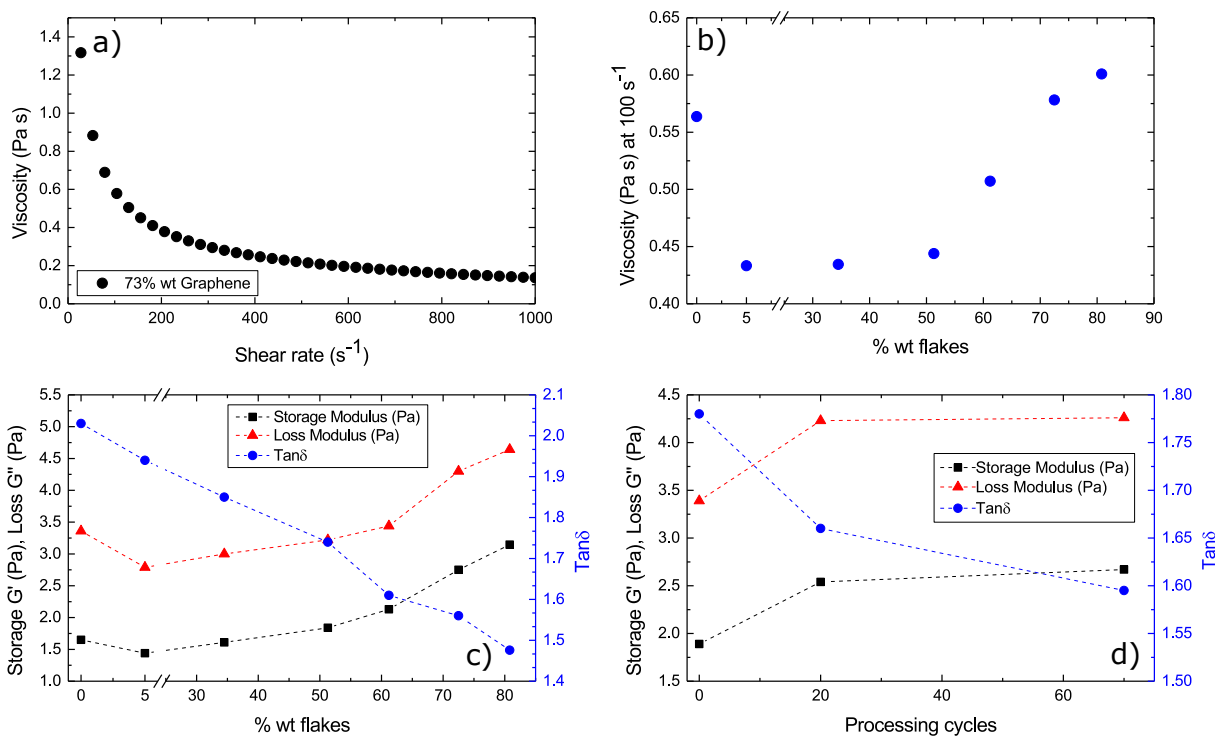


Figure 8: a) μ as a function of $\dot{\gamma}$ for an ink with 73wt% flakes, b) μ at $100s^{-1}$ for different flakes wt%. c,d) G' , G'' and $\tan\delta$ as a function of c) wt% flakes and d) processing cycles.

like (*i.e.* elastic) the material is at a given strain or frequency.¹⁰⁰ Fig.8c plots G' , G'' and $\tan\delta$ at 1% strain and frequency, checked from dynamic amplitude sweeps in order to be within the linear viscoelastic region (LVR). In LVR, G' and G'' are not stress or strain dependent¹⁰⁸ as a function of flake loading. The addition of 5 wt% flakes in CMC decreases both G' and G'' , which start to increase for loadings above 30 wt%. $\tan\delta$ decreases with flake loading, leading to a more solid-like behavior. We estimate G' , G'' and $\tan\delta$ also for inks containing flakes processed at different cycles, while keeping the flakes loading at $\sim 73\%$, Fig.8d. Both G' and G'' increase with processing cycles, while $\tan\delta$ decreases, indicating an increase of elastic behavior with processing.

For simplicity, blade coating is used to compare ink formulations. Inks are blade coated onto glass microscope slides (25x75mm) using a spacer to control h. The films are dried at $100^{\circ}C$ for 10 min to remove water. h depends on the wet film thickness, the total solid content wt% of the ink and the number of processing cycles. We investigate the effects of processing cycles, flake content and post-deposition annealing on R_S . This is measured in 4 different locations per sample using a four-

point probe. A profilometer (DektakXT, Bruker) is used to determine h for each point. In order to test the effect of the processing cycles, films are prepared from inks containing ~ 73 wt% flakes processed for 0, 5, 10, 30, 50, 70 and 100 cycles keeping the wet h constant (1mm). Fig.9a shows the effect of processing cycles on R_S and h . Without any processing, the films have $R_S \sim 77 \Omega/\square$ and $h = 35.8 \mu\text{m}$, corresponding to $\sigma \sim 3.6 \times 10^2 \text{ S/m}$. Microfluidization causes a drop in R_S and h . 10 cycles are enough to reach $\sim 10 \Omega/\square$ and $h \sim 25.6 \mu\text{m}$, corresponding to $\sigma \sim 3.9 \times 10^3 \text{ S/m}$. R_S does not change significantly between 10 and 100 cycles, while h slightly decreases. We get $\sigma \sim 4.5 \times 10^2 \text{ S/m}$ above 30 cycles.

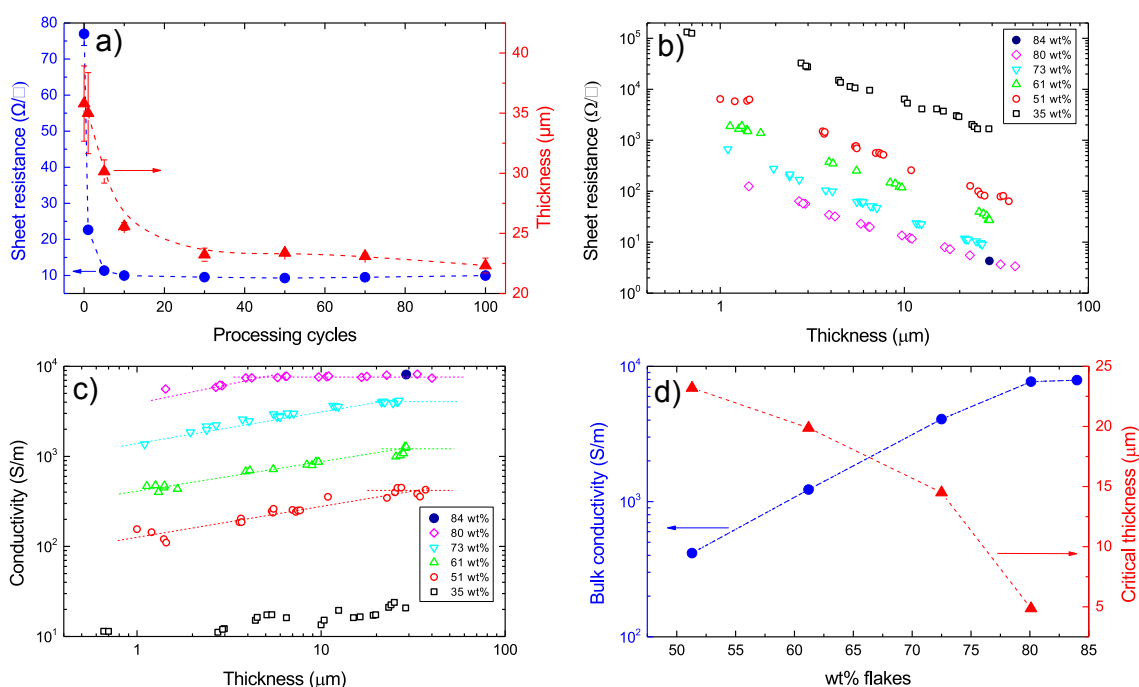


Figure 9: a) R_S and h as a function of processing cycles for a formulation with ~ 73 wt% flakes, b) R_S as a function of h for different wt% (70 cycles), c) σ as a function of h for different wt%, d) bulk σ and critical h as a function of wt% (70 cycles). All samples are dried for 10 min at 100°C .

The effect of flake loading for a fixed number of processing cycles (70) is investigated as follows. Dispersions with different loadings are prepared by increasing the flakes C between 1 and 100 g/L , whilst keeping the SDC (9 g/L) and CMC (10 g/L) constant. Films of different h are prepared by changing the spacer height during blade coating, leading to different wet and dry h . R_S and σ as a function of h are shown in Figs.9b,c. At ~ 34.5 wt% the flakes already form a percolative

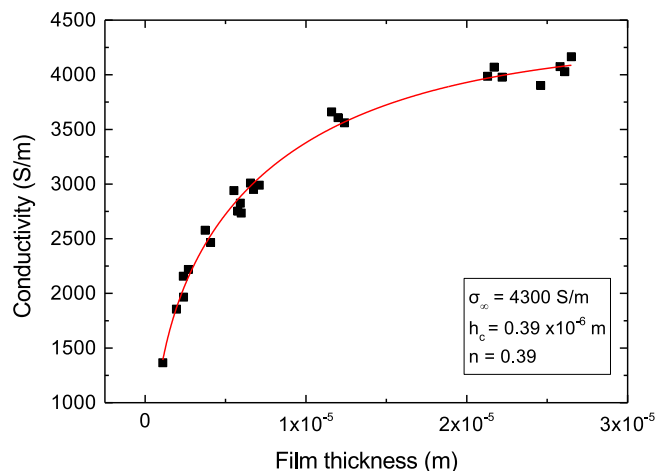


Figure 10: Fit of σ as a function of h according to Eq.3 for 73 wt%.

network within the CMC matrix and $\sigma \sim 15\text{-}20\text{S/m}$ is achieved (σ of cellulose derivative films is $< 10^{-8}\text{S/m}^{109}$). Fig.9c shows that, for a given composition, there is a critical h below which σ is thickness dependent. Above this, the bulk σ is reached. As shown in Fig.9c, for $\sim 80\text{wt}\%$ we get $\sigma \sim 7.7 \times 10^3\text{S/m}$ for $h > 4.5\mu\text{m}$. Higher loadings (84 wt%) do not increase σ further. Fig.9d indicates that the critical h where the bulk σ is reached drops from $\sim 20\mu\text{m}$ for 51 wt% to $\sim 4.5\mu\text{m}$ for 80 wt%. Coatings with $h > 4.5\mu\text{m}$ can be easily achieved using screen printing in a single printing pass. Fig.9c shows that σ is h dependent up to a critical point. In order to understand the effect of h on σ we adapt the percolation model of Ref. 110. The total area covered by non-overlapping flakes is A_f (e.g. for elliptical flakes $A_f = m\pi ab$ where m is the number of flakes and a [m] and b [m] are their half-axes lengths). The fractional area covered by the flakes (overlapping), with respect to the total area $S[\text{m}^2]$, can be evaluated as $q = 1 - p$, with $p = e^{-A_f/S}$ where q is the fractional area covered by the flakes.¹¹⁰ q coincides with A_f/S only when the flakes do not overlap. Denoting by $A_f h_f$ the total flakes volume and f the volume fraction of flakes in the films we have:

$$A_f h_f = f h S = -S h_f \ln p \quad (1)$$

σ follows a power law behavior of the form of:¹¹⁰

$$\sigma = k(q - q_c)^n \quad (2)$$

around the percolation threshold q_c ,¹¹⁰ and n is the electrical conductivity critical exponent above percolation. Eqs.1,2 give:

$$\sigma = \sigma_\infty \left[1 - e^{-\frac{(h_c - h)f}{h_f}} \right]^n \quad (3)$$

where $\sigma_\infty = ke^{-fnh_c/h_f}$ and h_c is the critical thickness corresponding to zero σ . σ as a function of h is fitted with Eq.3 in Fig.10 for $\sim 73\text{wt}\%$, *i.e.* $f=0.61$, giving $\sigma_\infty \sim 4.3 \times 10^3 \text{ S/m}$, $h_c = 0.39 \mu\text{m}$, $h_f \sim 7.58 \mu\text{m}$ and $n=0.39$.

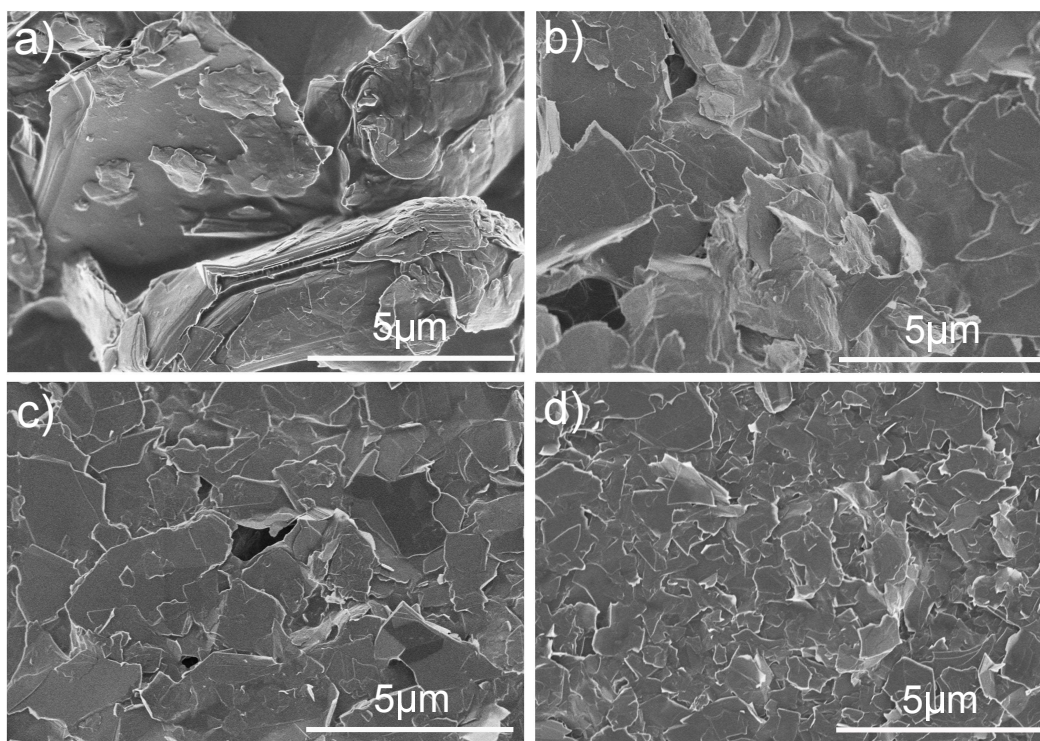


Figure 11: SEM images taken from coatings comprising a) starting graphite, b) after 1 cycle, c) after 5 cycles and d) after 100 cycles. The scale bar is $5 \mu\text{m}$.

Fig.11, shows SEM images of the coatings comprising the starting graphite (Fig.11a), after 1 (Fig.11b), 5 (Fig.11c) and 100 cycles (Fig.11d). Flake size reduction and platelet-like morphology is observed after the first cycle, Fig.11b. The samples have fewer voids compared to the starting

graphite, providing higher interparticle contact area and higher packing density, consistent with the h reduction (Fig.9a) and the increased σ . Whilst the packing density increase results in more pathways for conduction, the smaller flake size increases the number of inter-particle contacts. Then, R_S remains constant.

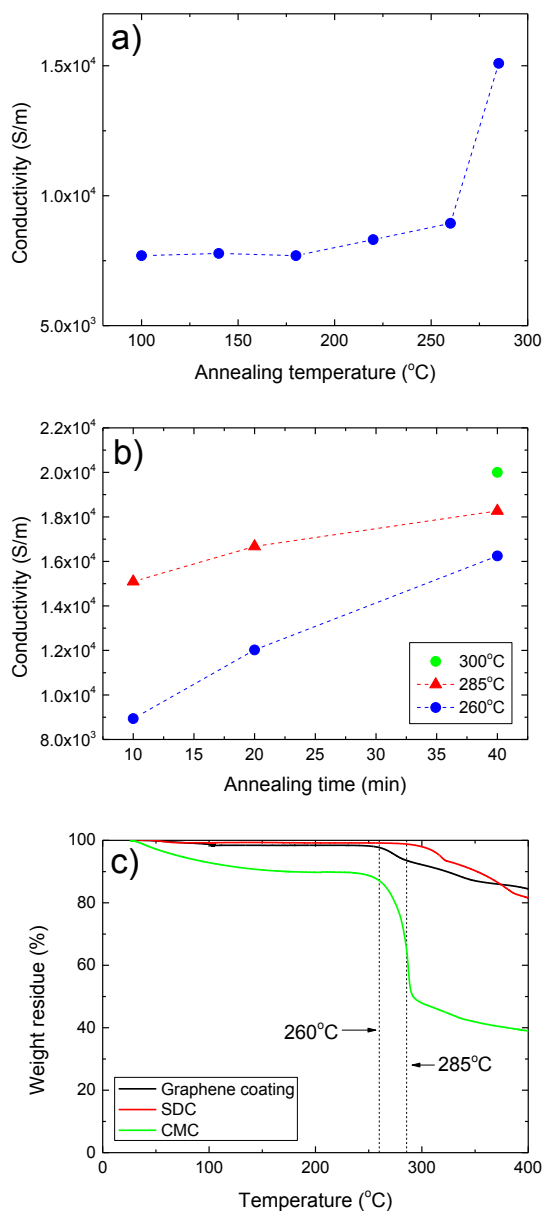


Figure 12: σ as a function of a) T and b) time. c) TGA thermograms from flakes coatings compared with with the SDC (powder) and the CMC (powder) components.

Post-deposition annealing is studied in blade-coated films for a~80wt% flakes after 70 cycles.

Fig.12a plots σ as a function of T. A three step regime can be seen. In the first (100-180°C) σ

1
2
3 is constant ($\sim 7.7 \times 10^3 \text{ S/m}$), above 180°C it increases, reaching $9 \times 10^3 \text{ S/m}$ at 260°C , followed by a
4
5 significant increase is at 285°C to $\sim 1.5 \times 10^4 \text{ S/m}$. Fig.12b shows the effect of annealing time at 260,
6
7 285 or 300°C . Either higher T or longer annealing times are required to increase σ .
8

9
10 TGA is then used to investigate the thermal stability of the films, Fig.12c. The thermogram of
11 CMC polymer reveals a 10% weight loss up to 200°C , due to water loss.¹¹¹ Fig.12 also shows that
12 50% of the CMC is decomposed at 285°C , while the SDC surfactant remains intact. Annealing at
13
14 300°C for 40min leads to films with $R_S \sim 2 \Omega/\square$ ($25 \mu\text{m}$) corresponding to $\sigma \sim 2 \times 10^4 \text{ S/m}$. This σ is
15
16 remarkable, given the absence of centrifugation, usually performed to remove the non-exfoliated
17
18 material, or washing steps to remove the non-conductive polymer and surfactant materials. The
19
20 SDC additive stabilizes the flakes against restacking through electrostatic repulsion forming a large
21
22 contact area per surfactant molecule.⁴⁰ CMC further stabilizes against restacking through electro-
23
24 steric repulsion.¹¹² Thus, R_S of our patterns is less than $2 \Omega/\square$, surpassing other reported printable
25
26 graphene inks.^{94,113–115} Our inks also could be exploited to prepare transparent conductive films,
27
28 by using grids. *e.g.* a grid with line width $\sim 100 \mu\text{m}$ and a pitch distance $\sim 2000 \mu\text{m}$, would give $\sim 90\%$
29
30 transparency, combined with low $R_S \sim 100 \Omega/\square$ at a thickness of $10 \mu\text{m}$.
31
32
33

34 The printability of the ink with $\sim 80\text{wt}\%$ flakes after 70 cycles is tested using a semi-automatic
35 flatbed screen printer (Kippax kpx 2012) and a Natgraph screen printer (Fig13a), both equipped
36
37 with screens with 120 mesh count per inch. Fig.13b shows a $29 \times 29 \text{ cm}^2$ print on paper with a line
38
39 resolution $\sim 100 \mu\text{m}$, Fig.13c. The pattern (Fig.13b) can be used as a capacitive touch pad in a sound
40
41 platform that translates touch into audio.¹¹⁶ The electronic module has a series of 12 contact pads
42
43 ($2.5 \text{ cm} \times 2.5 \text{ cm}$) on its underside that are interfaced to printed electronic pads on the paper surface.
44
45 This maintains a set-point charge on each of the printed capacitive touch pads. When a touch-pad
46
47 is touched, it undergoes an instantaneous discharge that is then identified by the electronics and a
48
49 corresponding sound is played. We measured the normalized resistance (resistance after bending/
50
51 resistance prior to bending) for up to 1400 cycles for a bending radius of 12.5 mm and observed a
52
53 change of less than 1%.
54
55
56
57
58
59
60

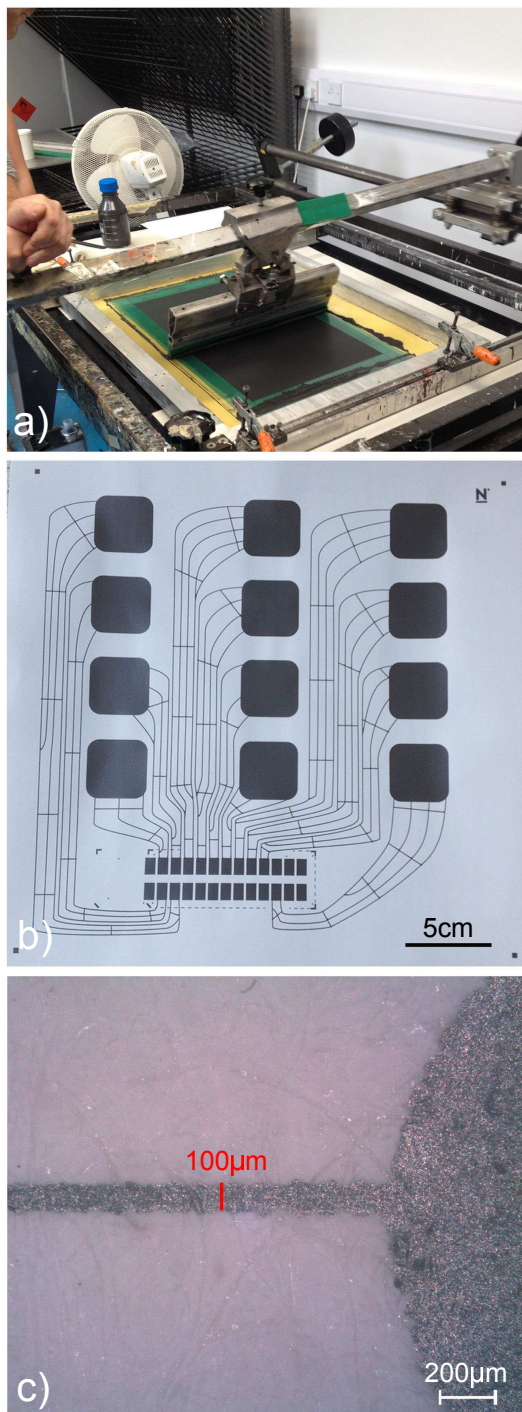


Figure 13: a) Demonstration of screen printing, b) capacitive touchpad design (29cmx29cm) printed on paper, c) the line resolution is 100µm.

Conclusions

We reported a simple and scalable route to exfoliate graphite. The resulting material can be used without any additional steps (washing or centrifugation) to formulate highly conductive inks with adjustable viscosity for high throughput printing. Conductivity as high as 2×10^4 S/m was demonstrated. Our approach enables the mass production of chemically unmodified flakes that can be used in inks, coatings and conductive composites for a wide range of applications.

Methods

Microfluidization process

In order to compare the microfluidization process with sonication or shear mixing it is important to elucidate its fluid dynamics. The mean velocity U [m/s] of the fluid inside the microchannel is:¹¹⁷

$$U = \frac{Q}{A} \quad (4)$$

where Q [m³/s] is the volumetric flow rate, defined as:¹¹⁸

$$Q = \frac{c_n V}{t} \quad (5)$$

where c_n is the number of cycles, V [m³] the volume of material (graphite and solvent) passing a point per unit time t [s] and A [m²] is the channel cross-sectional area, given by:

$$A = \pi \left(\frac{D_h}{2} \right)^2 \quad (6)$$

where $D_h=4A/P$ is the hydraulic diameter of the microchannel, with P the wetted perimeter (*i.e.* the part of the microchannel in contact with the flowing fluid¹¹⁷). For a batch of 0.18L it takes 1.93h to complete 70 cycles. Thus Eq.5 gives $Q=1.8 \times 10^{-6}$ m³/s. Eq.6 with $D_h \sim 87 \mu\text{m}$ ⁵⁸ gives

1
2
3
4
5
6
7
8
9
10
11
12
13
14
15
16
17
18
19
20
21
22
23
24
25
26
27
28
29
30
31
32
33
34
35
36
37
38
39
40
41
42
43
44
45
46
47
48
49
50
51
52
53
54
55
56
57
58
59
60

A=5940x10⁻¹²m². Thus, Eq.4 gives U~304m/s.

The Reynolds number, Re, can be used to determine the type of flow and it is given by:¹¹⁷

$$Re = \frac{\rho U D_h}{\mu} \quad (7)$$

where ρ [Kg/m³] is the liquid density. We typically use 50 up to 100g/L of graphite, which corresponds to a total density (mixture of graphite and water) of 1026 to 1052Kg/m³. μ [Pa s] is the dynamic viscosity ($\mu=\tau/\dot{\gamma}$, where τ [Pa] is the shear stress). We measure μ with a rotational rheometer in which a known $\dot{\gamma}$ is applied to the sample and the resultant torque (or τ) is measured.⁹⁹ We get $\mu \sim 1 \times 10^{-3}$ Pa s (20°C), similar to water.¹¹⁷ Thus, Eq.7 gives $Re \sim 2.7 \times 10^4$, which indicates that there is a fully developed turbulent flow inside the microchannel (there is a transition from laminar to turbulent flow in the 2000>Re>4000 range).¹¹⁹

The pressure losses inside the channel can be estimated by the Darcy-Weisbach equation,¹¹⁷ which relates the pressure drop, due to friction along a given length of pipe, to the average velocity of the fluid flow for an incompressible fluid:¹¹⁷

$$\Delta p = \frac{f_D L \rho U^2}{2D_h} \quad (8)$$

where Δp [Pa] is the pressure drop, L[m] is the pipe length, f_D is the Darcy friction factor, a dimensionless quantity used for the description of friction losses in pipe flow.¹¹⁷ The energy dissipation rate per unit mass ε [m²/s³] inside the channel can be written as:¹²⁰

$$\varepsilon = \frac{Q \Delta p}{\rho V_c} \quad (9)$$

where V_c is the volume of the liquid inside the microchannel. From Eqs.8,9 we can rewrite ε as:

$$\varepsilon = \frac{f_D U^3}{2D_h} \quad (10)$$

For $Re=2.7 \times 10^4$, we get $f_D \sim 0.052$ from the Moody chart,¹²¹ which links f_D , Re , and the relative roughness of the pipe (=absolute roughness/hydraulic diameter¹¹⁷). From Eqs.4,5,6, 10 we get $\varepsilon \sim 8.5 \times 10^9 \text{m}^2/\text{s}^3$. $\dot{\gamma}$ can then be estimated as:¹²²

$$\dot{\gamma} = \sqrt{\frac{\varepsilon}{\nu}} \quad (11)$$

where $\nu[\text{m}^2/\text{s}]$ is the kinematic viscosity,¹²² defined as $\nu = \mu/\rho \sim 1 \times 10^{-6} \text{m}^2/\text{s}$. From Eq.11 we get $\dot{\gamma} \sim 10^8 \text{s}^{-1}$, which is 4 orders of magnitude higher than that required to initiate graphite exfoliation.⁵² Thus, the exfoliation in the microfluidizer is primarily due to shear stress generated by the turbulent flow. In comparison, in a rotor-stator shear mixer, lower $\dot{\gamma} \sim 2 \times 10^4 - 1 \times 10^5 \text{s}^{-1}$ are achieved^{54,122,123} and only near the probe.⁵⁴ Thus, exfoliation does not take place in the entire batch uniformly.⁵² On the contrary, in a microfluidizer all the material is uniformly exposed to high shear forces.⁶²

Turbulent mixing is characterized by a near dissipationless cascade of energy,¹²² *i.e.* the energy is transferred from large (on the order of the size of the flow geometry considered) random, three-dimensional eddy type motions to smaller ones (on the order of the size of a fluid particle).¹¹⁷ This takes place from the inertial subrange (IS) of turbulence where inertial stresses dominate over viscous stresses, down to the Kolmogorov length,¹²⁴ $\eta[\text{m}]$, *i.e.* the length-scale above which the system is in the turbulence IS, and below which it is in the viscous subrange (VS), where turbulence energy is dissipated by heat.^{122,125} η can be calculated as:¹²⁴

$$\eta = \left(\frac{\nu^3}{\varepsilon} \right)^{\frac{1}{4}} \quad (12)$$

From $\nu \sim 1 \times 10^{-6} \text{m}^2/\text{s}$ and Eq.9, we get $\eta \sim 103 \text{nm}$ for microfluidization in water. Since our starting graphitic particles are much larger ($> \mu\text{m}$) than η , exfoliation occurs in the turbulence IS rather than VS. In comparison, in a kitchen blender $\eta = 6 \mu\text{m}$,¹²⁶ thus exfoliation occurs in the VS, *i.e.* the energy is dissipated through viscous losses, rather than through particle disruption. During microfluidization, in the IS, the main stress contributing to exfoliation is due to pressure fluctuations,

1
2
3 *i.e.* the graphite is bombarded with turbulent eddies. This stress, τ_{IS} [Pa], can be estimated as:¹²²
4
5

$$\tau_{IS} \sim \rho(\epsilon d_g)^{\frac{2}{3}} \quad (13)$$

6
7
8
9
10 where d_g is the diameter of a sphere of equivalent volume to the flakes. For $d_g=0.1$ to $27\mu\text{m}$, τ_{IS} is
11 in the ~ 0.1 - 4MPa range. The dynamic pressure also breaks the flakes, as well as exfoliating them.
12
13 For length scales $< \eta$, we are in the VS and the stress applied on the flakes, τ_{VS} , can be estimated
14
15 as:¹²²
16
17

$$\tau_{VS} \sim \mu \sqrt{\frac{\epsilon}{\nu}} \quad (14)$$

18
19
20 which gives $\tau_{VS} \sim 0.1\text{MPa}$. Thus, the stresses applied on the flakes in the IS are much higher than
21 in the VS, where energy is lost by heat. This can lead to more defects in the basal plane. The
22 Kolmogorov length can be tuned, Eq.12, by either increasing the kinematic viscosity of the disper-
23 sion or decreasing the energy dissipation rate, thus extending the viscous subrange of turbulence
24 realizing a milder exfoliation.
25
26
27
28
29
30
31

32 In microfluidization, the energy density E/V [J/m^3], (where E [J] is the energy) equates the pres-
33 sure differential,⁶¹ due to very short residence times $\sim 10\text{s}^{-4}$,⁶¹ *i.e.* the time the liquid spends in the
34 microchannel. Therefore, for a processing pressure $\sim 207\text{MPa}$, $E/V = 207\text{MPa} = 2.07 \times 10^8 \text{J}/\text{m}^3$. For
35 this total energy input per unit volume, the flakes production rate $P_r = VC/t$ [g/h] for a typical batch
36 of $V=0.18\text{L}$ and $t=1.93\text{h}$ (for 70 cycles), is $P_r \sim 9.3\text{g}/\text{h}$, with starting graphite concentration ~ 100
37 g/L using a lab-scale system. Scale-up can be achieved by increasing Q , using a number of paral-
38 lel microchannels,⁵⁸ which decreases the time required to process a given V and c_n (Eq.5). With
39 shorter time, P_r increases. Large scale microfluidizers can achieve flow rates $\sim 12\text{L}/\text{min}$ ⁵⁸ at pro-
40 cessing pressure $\sim 207\text{MPa}$, which correspond to $P_r = CQ/c_n \sim 1\text{Kg}/\text{h}$ ($\sim 9\text{ton}$ per year, $\sim 90\text{k}$ liters of
41 ink per year) in an industrial system using 70 process cycles and $C=100\text{g}/\text{L}$.
42
43
44
45
46
47
48
49
50
51
52
53
54

55 Acknowledgement

56
57 We acknowledge funding from EU Graphene Flagship, ERCs Grants Hetero2D, HiGRAPHINK,
58
59
60

1
2
3 3DIMAGEEPSRC, ESTEEM2, BIHSNAM, KNOTOUGH, SILKENE, EPSRC Grants EP/K01711X/1,
4 EP/K017144/1, EP/N010345/1, a Vice Chancellor award from the University of Cambridge, a Ju-
5
6
7
8
9
10
11
12
13
14
15
16
17
18
19
20
21
22
23
24
25
26
27
28
29
30
31
32
33
34
35
36
37
38
39
40
41
42
43
44
45
46
47
48
49
50
51
52
53
54
55
56
57
58
59
60

We thank Chris Jones for useful discussions, and Imerys Graphite & Carbon for graphite powders.

References

- (1) Jung, S.; Hoath, S. D.; Martin, G. D.; Hutchings, I. M. Inkjet Printing Process for Large Area Electronics. In *Large Area and Flexible Electronics*; Caironi, M.; Noh, Y.-Y. Eds; Wiley-VCH Verlag GmbH & Co. KGaA Boschstr. 12, 69469 Weinheim, Germany, 2015; pp 317-341.
- (2) Leppäniemi, J.; Huttunen, O.-H.; Majumdar, H.; Alastalo, A. Flexography-Printed In₂O₃ Semiconductor Layers for High-Mobility Thin-Film Transistors on Flexible Plastic Substrate. *Adv. Mater.* **2015**, *27*, 7168-7175.
- (3) Lau, P. H.; Takei, K.; Wang, C.; Ju, Y.; Kim, J.; Yu, Z.; Takahashi, T.; Cho, G.; Javey, A. Fully Printed, High Performance Carbon Nanotube Thin-Film Transistors on Flexible Substrates. *Nano Lett.* **2013**, *13*, 3864-3869.
- (4) Krebs, F. C.; Fyenbob, J.; Jørgensen, M. Product Integration of Compact Roll-to-Roll Processed Polymer Solar Cell Modules: Methods and Manufacture using Flexographic Printing, Slot-die Coating and Rotary Screen Printing. *J. Mater. Chem.* **2010**, *20*, 8994-9001.
- (5) Dearden, A. L.; Smith, P. J.; Shin, D.-Y.; Reis, N.; Derby, B.; O'Brien, P. A Low Curing Temperature Silver Ink for Use in Ink-Jet Printing and Subsequent Production of Conductive Tracks. *Macromol. Rapid Commun.* **2005**, *26*, 315-318.
- (6) Magdassi, S.; Grouchko, M.; Kamyshny, A. Copper Nanoparticles for Printed Electronics: Routes Towards Achieving Oxidation Stability. *Materials* **2010**, *3*, 4626-4638.

- 1
2
3
4 (7) Wang, J.; Pamidi, P. V. A. Sol-Gel-Derived Gold Composite Electrodes. *Anal. Chem.* **1997**,
5 69, 4490-4494.
6
7
8
9 (8) Jeong, S.; Woo, K.; Kim, D.; Lim, S.; Kim, J. S.; Shin, H.; Xia, Y.; Moon, J. Controlling the
10 Thickness of the Surface Oxide Layer on Cu Nanoparticles for the Fabrication of Conductive
11 Structures by Ink-Jet Printing. *Adv. Funct. Mater.* **2008**, *18*, 679-686.
12
13
14
15 (9) Grouchko, M.; Kamyshny, A.; Mihailescu, C. F.; Anghel, D. F.; Magdassi, S. Conductive
16 Inks with a Built-In Mechanism That Enables Sintering at Room Temperature. *ACS Nano*
17 **2011**, *5*, 3354-3359.
18
19
20
21
22 (10) Rida, A.; Yang, L.; Vyas, R.; Tentzeris, M. M. Conductive Inkjet-Printed Antennas on Flex-
23 ible Low-Cost Paper-Based Substrates for RFID and WSN Applications. *IEEE Antennas*
24 *Propag. Mag.* **2009**, *51*, 13-23.
25
26
27
28
29 (11) Kim, Y.; Lee, B.; Yang, S.; Byun, I.; Jeong, I.; Cho, S. M. Use of Copper Ink for Fabricating
30 Conductive Electrodes and RFID Antenna Tags by Screen Printing. *Curr. Appl. Phys.* **2012**,
31 *12*, 473-478.
32
33
34
35
36 (12) Lucera, L.; Kubis, P.; Fecher, F. W.; Bronnbauer, C.; Turbiez, M.; Forberich, K.; Ameri,
37 T.; Egelhaaf, H.-J.; Brabec, C. J. Guidelines for Closing the Efficiency Gap between Hero
38 Solar Cells and Roll-To-Roll Printed Modules. *Energy Technol.* **2015**, *3*, 373-384.
39
40
41
42
43 (13) Huang, X.; Leng, T.; Zhang, X.; Chen, J. C.; Chang, K. H.; Geim, A. K.; Novoselov, K.
44 S.; Hu, Z. Binder-free Highly Conductive Graphene Laminate for Low Cost Printed Radio
45 Frequency Applications *Appl. Phys. Lett.* **2015**, *106*, 203105.
46
47
48
49
50 (14) Hösel, M.; Søndergaard, R. R.; Angmo, D.; Krebs, F. C. Comparison of Fast Roll-to-Roll
51 Flexographic, Inkjet, Flatbed, and Rotary Screen Printing of Metal Back Electrodes for
52 Polymer Solar Cells. *Adv Eng Mater* **2013**, *15*, 995-1001.
53
54
55
56
57
58
59
60

- 1
2
3
4 (15) Sommer-Larsen, P.; Jørgensen, M.; Søndergaard, R. R.; Hösel, M.; Krebs, F. C. It is all in the
5 Pattern-Dependent High-Efficiency Power Extraction from Polymer Solar Cells through High-Voltage
6 Serial Connection. *Energy Technol.* **2013**, *1*, 15-19.
7
8
9
10 (16) Krebs, F. C.; Espinosa, N.; Hösel, M.; Søndergaard, R. R.; Jørgensen, M. 25th Anniversary
11 Article: Rise to Power of OPV-Based Solar Parks. *Adv. Mater.* **2014**, *26*, 29-39.
12
13
14 (17) Barker M. J. Screen inks. In *The Printing Ink Manual*, Leach, R. H.; Pierce, R. J.; Hickman,
15 E. P.; Mackenzie, M. J.; Smith, H. G.; Eds.; Springer, The Netherlands, 2007; pp 599-634.
16
17
18 (18) Khan, S.; Lorenzelli, L.; Dahiya, R. S. Technologies for Printing Sensors and Electronics
19 Over Large Flexible Substrates: A Review. *IEEE Sens J* **2015**, *15* 3164-3185.
20
21
22 (19) Tobjörk, D.; Österbacka, R. Paper Electronics. *Adv. Mater.* **2011**, *23*, 1935-1961.
23
24
25 (20) Merilampi, S.; Laine-Ma, T.; Ruuskanen, P. The Characterization of Electrically Conductive
26 Silver Ink Patterns on Flexible Substrates *Microelectron. Reliab.* **2009**, *49*, 782-790.
27
28
29 (21) Hyun, W. J.; Lim, S.; Ahn, B. Y.; Lewis, J. A.; Frisbie, C. D.; Francis, L. F. Screen Printing
30 of Highly Loaded Silver Inks on Plastic Substrates Using Silicon Stencils. *ACS Appl. Mater.*
31 *Interfaces* **2015**, *7*, 12619-12624.
32
33
34 (22) Silverprice <http://silverprice.org> (accessed Nov 7 2016)
35
36
37 (23) Infomine <http://infomine.com/investment/metal-prices/copper/5-year/> (accessed Nov 7
38 2016)
39
40
41 (24) Kamyshny, A.; Magdassi, S.; Conductive Nanomaterials for Printed Electronics. *Small*
42 **2014**, *10*, 3515-3535
43
44
45 (25) Lachkar, A.; Selmani, A.; Sacher, E.; Leclerc, M.; Mokhliss R. Metallization of Poly-
46 thiophenes I. Interaction of Vapor-Deposited Cu, Ag and Au with Poly(3-hexylthiophene)
47 (P3HT) *Synthetic Met* **1994**, *66*, 209-215.
48
49
50
51
52
53
54
55
56
57
58
59
60

- 1
2
3
4 (26) Zhang H. X-ray Microbeam Analysis of Electromigration in Copper Interconnects, In *Electromigration in thin films and electronic devices, Materials and reliability*, Kim, C.-U., Ed.;
5
6 *Woodhead Publishing Limited, Cambridge, UK 2011; pp 97-110.*
7
8
9
10
11 (27) Rösch, R.; Tanenbaum, D. M.; Jørgensen, M.; Seeland, M.; Bärenklau, M.; Hermenau, M.;
12 Voroshazi, E.; Lloyd, M. T.; Galagan, Y.; Zimmermann, B.; Würfel, U.; Hösel, M.; Dam,
13 H. F.; Gevorgyan, S. A.; Kudret, S.; Maes, W.; Lutsen, L.; Vanderzande, D.; Andriessen,
14 R.; Teran-Escobar, G. Investigation of the Degradation Mechanisms of a Variety of Organic
15 Photovoltaic Devices by Combination of Imaging techniques—the ISOS-3 Inter-laboratory
16 Collaboration. *et al. Energy Environ. Sci.* **2012**, *5*, 6521-6540.
17
18
19
20
21
22
23 (28) Søndergaard, R. R.; Espinosa, N.; Jørgensen, M.; Krebs, F. C. Efficient Decommissioning
24 and Recycling of Polymer Solar Cells: justification for use of silver. *Energy Environ. Sci.*
25 **2014**, *7*, 1006-1012.
26
27
28
29
30 (29) Fahmy, B.; Cormier, S. A. Copper Oxide Nanoparticles Induce Oxidative Stress and Cyto-
31 toxicity in Airway Epithelial Cells. *Toxicol. in Vitro* **2009**, *23*, 1365-1371.
32
33
34
35 (30) Ahamed, M.; Siddiqui, M. A.; Akhtar, M. J.; Ahmad, I.; Pant, A. B.; Alhadlaq, H. A. Geno-
36 toxic Potential of Copper Oxide Nanoparticles in Human Lung Epithelial Cells. *Biochem.*
37 *Biophys. Res. Commun.* **2010**, *396*, 578-583.
38
39
40
41
42 (31) Karlsson, H. L.; Cronholm, P.; Gustafsson, J.; Möller, L. Copper Oxide Nanoparticles Are
43 Highly Toxic: A Comparison between Metal Oxide Nanoparticles and Carbon Nanotubes.
44 *Chem. Res. Toxicol.* **2008**, *21*, 1726-1732.
45
46
47
48
49 (32) Statista <http://statista.com> (accessed Nov 7 2016)
50
51
52 (33) Conductive Carbon Ink C2130925D1 <http://gwent.org> (accessed Nov 7 2016)
53
54
55 (34) Henkel Adhesive Technologies, Low-resistivity, screen-printable, carbon ink, LOCTITE
56 EDAG PF 407C E&C <http://henkel-adhesives.com/> (accessed Nov 7 2016)
57
58
59
60

- 1
2
3
4 (35) DuPont 7102 and BQ242 Conductive Carbon Inks, <http://dupont.com> (accessed Nov 7 2016)
- 5
6
7 (36) Ferrari, A. C.; Bonaccorso, F.; Fal'ko, V.; Novoselov, K. S.; Roche, S.; Bøggild, P.; Borini,
8 S.; Koppens, F. H. L.; Palermo, V.; Pugno, N.; Garrido, J. A.; Sordan, R.; Bianco, A.;
9 Ballerini, L.; Prato, M.; Lidorikis, E.; Kivioja, J.; Marinelli, C.; Ryhänen, T.; Morpurgo A.
10 *et al.* Science and Technology Roadmap for Graphene, Related Two-dimensional Crystals,
11 and Hybrid Systems. *Nanoscale* **2015**, *7*, 4598-4810.
- 12
13
14
15
16
17 (37) Hernandez, Y.; Nicolosi, V.; Lotya, M.; Blighe, F. M.; Sun, Z.; De, S.; McGovern, I. T.; Hol-
18 land, B.; Byrne, M.; Gun'Ko, Y. K.; Boland, J. J.; Niraj, P.; Duesberg, G.; Krishnamurthy,
19 S.; Goodhue, R.; Hutchison, J.; Scardaci, V.; Ferrari, A. C.; Coleman, J. N., High-Yield
20 Production of Graphene by Liquid-Phase Exfoliation of Graphite *Nat. Nanotechnol.* **2008**,
21 *3*, 563-568.
- 22
23
24
25
26
27 (38) Vallés, C.; Drummond, C.; Saadaoui, H.; Furtado, C. A.; He, M.; Roubeau, O.; Ortolani,
28 L.; Monthieux, M.; Pénicaud, A. Solutions of Negatively Charged Graphene Sheets and
29 Ribbons. *J. Am. Chem. Soc.* **2008**, *130*, 15802-15804.
- 30
31
32
33
34 (39) Khan, U.; O'Neill, A.; Lotya, M.; De, S.; Coleman, J. N. High-Concentration Solvent
35 Exfoliation of Graphene. *Small* **2010**, *6*, 864-871.
- 36
37
38
39 (40) Hasan, T.; Torrisi, F.; Sun, Z.; Popa, D.; Nicolosi, V.; Privitera, G.; Bonaccorso, F.; Ferrari,
40 A. C. Solution-phase Exfoliation of Graphite for Ultrafast Photonics. *Phys. Status Solidi B*
41 **2010**, *247*, 2953-2957.
- 42
43
44
45 (41) Hernandez, Y.; Lotya, M.; Rickard, D.; Bergin, S. D.; Coleman, J. N. Measurement of Mul-
46 ticomponent Solubility Parameters for Graphene Facilitates Solvent Discovery. *Langmuir*
47 **2010**, *26*, 3208-3213.
- 48
49
50
51 (42) Bourlinos, A. B.; Georgakilas, V.; Zboril, R.; Steriotis, T. A.; Stubos, A. K. Liquid-Phase
52 Exfoliation of Graphite Towards Solubilized Graphenes. *Small* **2009**, *5*, 1841-1845.
- 53
54
55
56
57
58
59
60

- 1
2
3
4 (43) Lotya, M.; Hernandez, Y.; King, P. J.; Smith, R. J.; Nicolosi, V.; Karlsson, L. S.; Blighe,
5 F. M.; De, S.; Wang, Z.; McGovern, I. T.; Duesberg, G. S.; Coleman, J. N. Liquid Phase
6 Production of Graphene by Exfoliation of Graphite in Surfactant/Water Solutions. *J. Am.*
7 *Chem. Soc.* **2009**, *131*, 3611-3620.
8
9
10
11
12 (44) Bonaccorso, F.; Lombardo, A.; Hasan, T.; Sun, Z.; Colombo, L.; Ferrari, A. C. Production
13 and Processing of Graphene and 2d Crystals. *Mater. Today* **2012**, *15*, 564-589.
14
15
16
17 (45) Torrisi, F.; Hasan, T.; Wu, W.; Sun, Z.; Lombardo, A.; Kulmala, T. S.; Hsieh, G.-W.; Jung,
18 S.; Bonaccorso, F.; Paul, P. J.; Chu, D.; Ferrari, A. C. Inkjet-Printed Graphene Electron-
19 ics. *ACS Nano* **2012**, *6*, 2992-3006.
20
21
22
23
24 (46) Santos, H. M.; Lodeiro, C.; Capelo-Martinez J. L., The Power of Ultrasound. In *Ultra-*
25 *sound in Chemistry*, Capelo-Martinez, J. L., Ed.; Wiley-VCH Verlag GmbH & Co. KGaA,
26 Weinheim 2009; pp 1-15.
27
28
29
30
31 (47) Nascentes, C. C.; Korn, M.; Sousa, C. S.; Arruda, M. A. Z. Use of Ultrasonic Baths for
32 Analytical Applications: A New Approach for Optimisation Conditions. *J. Braz. Chem.*
33 *Soc.* **2001**, *12*, 57-63.
34
35
36
37
38 (48) Chivate, M. M.; Pandit, A. B. Quantification of Cavitation Intensity in Fluid Bulk. *Ultrason.*
39 *Sonochem.* **1995**, *2*, 19-25.
40
41
42
43 (49) McClements, D. J., Homogenization devices. In *Food Emulsions Principles, Practices, and*
44 *Techniques* CRC Press, Boca Raton London New York Washington, D.C., 2005; pp 249-260
45
46
47
48 (50) Secor, E. B.; Prabhumirashi, P. L.; Punbekar, K.; Geier, M. I.; Hersam, M. C. Inkjet
49 Printing of High Conductivity, Flexible Graphene Patterns. *J. Phys. Chem. Lett.* **2013**, *4*,
50 1347-1351.
51
52
53
54
55 (51) Hyun, W. J.; Secor, E. B.; Hersam, M. C.; Frisbie, C. D.; Francis, L. F. High-Resolution
56
57
58
59
60

- 1
2
3 Patterning of Graphene by Screen Printing with a Silicon Stencil for Highly Flexible Printed
4 Electronics. *Adv. Mater.* **2015**, *27*, 109-115.
5
6
7
8
9 (52) Paton, K. R.; Varrla, E.; Backes, C.; Smith, R. J.; Khan, U.; O'Neill, A.; Boland, C.; Lotya,
10 M.; Istrate, O. M.; King, P.; Higgins, T.; Barwich, S.; May, P.; Puczkarski, P.; Ahmed, I.;
11 Moebius, M.; Pettersson, H.; Long, E.; Coelho, J.; O'Brien, S. E. *et al.* Scalable Production
12 of Large Quantities of Defect-free Few-Layer Graphene by Shear Exfoliation in Liquids.
13 *Nat. Mater.* **2014**, *13*, 624-630.
14
15
16
17
18
19 (53) Barnes, H. A., What is Flow and Deformation?. In *A Handbook of Elementary Rheology*;
20 Institute of Non-Newtonian Fluid Mechanics, University of Wales, 2004; pp 5-10
21
22
23
24 (54) Atiemo-Obeng V. A.; Calabrese, R. V. Rotor-Stator Mixing Devices. In *Handbook of In-*
25 *dustrial Mixing: Science and Practice*; Paul, E. L.; Atiemo-Obeng, V. A.; Kresta S. M.,
26 Eds.; John Wiley & Sons, Inc., Hoboken, New Jersey, 2004; pp 479-505
27
28
29
30
31 (55) Wang, J.; Manga, K. K.; Bao, Q.; Loh, K. P. High-Yield Synthesis of Few-Layer Graphene
32 Flakes through Electrochemical Expansion of Graphite in Propylene Carbonate Electrolyte.
33 *J. Am. Chem. Soc.* **2011**, *133*, 8888-8891.
34
35
36
37
38 (56) Panagiotou, T.; Mesite, S. V.; Bernard, J. M.; Chomistek, K. J.; Fisher, R. J. Production of
39 Polymer Nanosuspensions Using Microfluidizer (R) Processor Based Technologies. *NSTI-*
40 *Nanotech* **2008**, *1*, 688-691.
41
42
43
44
45 (57) Goldberg S., Mechanical/Physical Methods of Cell Disruption and Tissue. In *2D PAGE:*
46 *Sample Preparation and Fractionation*, A. Posch, Ed; Totowa, NJ Humana Press, 2008; pp
47 3-22.
48
49
50
51
52 (58) Microfluidics International Corporation <http://www.microfluidicscorp.com/> (accessed Nov
53 7 2016)
54
55
56
57
58
59
60

- 1
2
3
4 (59) Lajunen, T.; Hisazumi, K.; Kanazawa, T.; Okada, H.; Seta, Y.; Yliperttula, M.; Urtti, A.;
5 Takashima, Y. Topical Drug Delivery to Retinal Pigment Epithelium with Microfluidizer
6 Produced Small Liposomes. *Eur J Pharm Sci* **2014**, *62*, 23-32.
7
8
9
10 (60) Tang, S. Y.; Shridharan, P.; Sivakumar, M. Impact of Process Parameters in the Generation
11 of Novel Aspirin Nanoemulsions Ū Comparative Studies Between Ultrasound Cavitation
12 and Microfluidizer. *Ultrason Sonochem* **2013**, *20*, 485-497.
13
14
15
16
17 (61) Jafari, S. M.; He, Y.; Bhandari, B. Production of Sub-micron Emulsions by Ultrasound and
18 Microfluidization Techniques. *J Food Eng* **2007**, *82*, 478-488.
19
20
21
22 (62) Panagiotou, T.; Bernard, J. M.; Mesite, S. V. Deagglomeration and Dispersion of Carbon
23 Nanotubes Using Microfluidizer (R) High Shear Fluid Processors. *NSTI-Nanotech* **2008**, *1*,
24 39-42.
25
26
27
28
29 (63) dos Reis Benatto, G. A.; Roth, B.; Madsen, M. V.; Hösel, M.; Søndergaard, R. R.; Jørgensen,
30 M.; Krebs, F. C. Carbon: The Ultimate Electrode Choice for Widely Distributed Polymer
31 Solar Cells. *Adv. Energy Mater.* **2014**, *4* 1400732.
32
33
34
35
36 (64) Gomes H. L. Organic Field-Effect Transistors. In *Organic and Printed Electronics Funda-*
37 *mentals and Applications*, Nisato, G.; Lupo D.; Ganz S., Eds.; CRC Press 2016; pp147-197.
38
39
40
41 (65) Imerys <http://www.imerys-graphite-and-carbon.com/> (accessed Nov 7 2016)
42
43
44 (66) Kouroupis-Agalou, K.; Liscio, A.; Treossi, E.; Ortolani, L.; Morandi, V.; Pugno, N. M.;
45 Palermo, V. Fragmentation and Exfoliation of 2-dimensional Materials: A Statistical Ap-
46 proach. *Nanoscale* **2014**, *6*, 5926-5933.
47
48
49
50
51 (67) Moeck, P.; Rouvimov, S.; Rauch, E. F.; Véron, M.; Kirmse, H.; Häusler I.; Neumann,
52 W.; Bultreys, D.; Maniette, Y.; Nicolopoulos, S. High Spatial Resolution Semi-automatic
53 Crystallite Orientation and Phase Mapping of Nanocrystals in Transmission Electron Mi-
54 croscopes. *Cryst. Res. Technol.* **2011**, *46*, 589-606.
55
56
57
58
59
60

- 1
2
3
4 (68) Nanomegas <http://nanomegas.com> (accessed Nov 7 2016)
5
6
7 (69) Gammer, C.; Burak-Ozdol, V.; Liebscher, C. H.; Minor, A. Diffraction Contrast Imaging
8 Using Virtual Apertures. *Ultramicroscopy* **2015**, *155*, 1-10.
9
10
11 (70) Punckt, C.; Muckel, F.; Wolff, S.; Aksay, I. A.; Chavarin, C. A.; Bacher, G.; Mertin, W.
12 The Effect of Degree of Reduction on the Electrical Properties of Functionalized Graphene
13 Sheets. *Appl. Phys. Lett.* **2013**, *102*, 023114-023114-5.
14
15
16 (71) ASTM E1131-08 Standard Test Method for Compositional Analysis by Thermogravimetry
17 (West Conshohocken, PA, 2014).
18
19
20 (72) Shirley, D. A. High-Resolution X-Ray Photoemission Spectrum of the Valence Bands of
21 Gold. *Phys. Rev. B* **1972**, *5*, 4709-4714.
22
23
24 (73) Welham, N.J.; Williams, J.S. Extended Milling of Graphite and Activated Carbon. *Carbon*
25 **1998**, *36*, 1309-1315.
26
27
28 (74) Benson, J.; Xu, Q.; Wang, P.; Shen, Y.; Sun, L.; Wang, T.; Li, M.; Papakonstantinou, P.
29 Tuning the Catalytic Activity of Graphene Nanosheets for Oxygen Reduction Reaction *via*
30 Size and Thickness Reduction. *ACS Appl. Mater. Interfaces* **2014**, *6*, 19726-19736.
31
32
33 (75) ASTM E1078-14 Standard Guide for Specimen Preparation and Mounting in Surface Anal-
34 ysis (West Conshohocken, PA, 2014).
35
36
37 (76) Moulder, J. F.; Stickle, W. F.; Sobol, P. E.; Bomben, K. D. Handbook of X-ray Photoelectron
38 Spectroscopy; Perkin-Elmer: Eden Prairie, MN, 1992.
39
40
41 (77) Phaner-Goutorbe, M.; Sartre, A.; Porte, L. Soft Oxidation of Graphite Studied by XPS and
42 STM. *Microsc. Microanal. Microstruct.* **1994**, *5*, 283-290.
43
44
45 (78) Briggs, D.; Seah, M. P., Practical Surface Analysis, Auger and X-Ray Photoelectron Spec-
46 troscopy, Wiley, 1990.
47
48
49
50
51
52
53
54
55
56
57
58
59
60

- 1
2
3
4 (79) Yang, D.; Velamakannia, A.; Bozoklu, G.; Park, S.; Stoller, M.; Piner, R. D.; Stankovich,
5 S.; Jung, I.; Field, D. A.; Ventrice, Jr. C. A.; Ruoff, R. S. Chemical Analysis of Graphene
6 Oxide Films after Heat and Chemical Treatments by X-ray Photoelectron and Micro-Raman
7 Spectroscopy. *Carbon* **2009**, *47*, 145-152.
8
9
10
11
12 (80) Drewniak, S.; Muzyka, R.; Stolarczyk A.; Pustelny T.; Kotyczka-Morańska M.; Setkiewicz
13 M. Studies of Reduced Graphene Oxide and Graphite Oxide in the Aspect of Their Possible
14 Application in Gas Sensors. *Sensors (Basel)* **2016**, *16*, 103.
15
16
17
18
19 (81) Haubner, K.; Murawski, J.; Olk, P.; Eng, L. M.; Ziegler, C.; Adolphi, B.; Jaehne, E. The
20 Route to Functional Graphene Oxide. *Chemphyschem* **2010**, *11*, 2131-2139.
21
22
23
24 (82) Tuinstra, F.; Koenig, J. L. Raman Spectrum of Graphite. *J. Chem. Phys.* **1970**, *53*, 1126-
25 1130.
26
27
28
29 (83) Ferrari, A. C.; Robertson, J. Interpretation of Raman spectra of disordered and amorphous
30 carbon. *Phys. Rev. B* **2000**, *61*, 14095-14107.
31
32
33
34 (84) Thomsen, C.; Reich S. Double Resonant Raman Scattering in Graphite. *Phys. Rev. Lett.*
35 **2000**, *85*, 5214-5217.
36
37
38
39 (85) Baranov, A. V.; Bekhterev, A. N.; Bobovich, Ya. S.; Petrov, V. I. Interpretation of Certain
40 Characteristics in Raman Spectra of Graphite and Glassy Carbon. *Opt. Spectroscopy* **1987**,
41 *62*, 612-616.
42
43
44
45 (86) Pocsik, I.; Hundhausen, M.; Koos, M.; Ley, L. Origin of the D Peak in the Raman Spectrum
46 of Microcrystalline Graphite. *J. Non-Cryst. Solids* **1998**, *227*, 1083-1086.
47
48
49
50 (87) Piscanec, S.; Lazzeri, M.; Mauri, F.; Ferrari, A. C.; Robertson, J. Kohn Anomalies and
51 Electron-Phonon Interactions in Graphite. *Phys. Rev. Lett.* **2004**, *93*, 185503.
52
53
54
55 (88) Ferrari, A. C.; Meyer, J. C.; Scardaci, V.; Casiraghi, C.; Lazzeri, M.; Mauri, F.; Piscanec,
56
57
58
59
60

- 1
2
3 S.; Jiang, D.; Novoselov, K. S.; Roth, S.; Geim A. K. Raman Spectrum of Graphene and
4 Graphene Layers. *Phys. Rev. Lett.* **2006**, *97*, 187401.
5
6
7
8
9 (89) Basko D. M.; Piscanec S.; Ferrari A. C. Electron-electron Interactions and Doping Depen-
10 dence of the Two-Phonon Raman Intensity in Graphene. *Phys. Rev. B* **2009**, *80*, 165413.
11
12
13 (90) Ferrari, A. C.; Basko, D. M. Raman Spectroscopy as a Versatile Tool for Studying the
14 Properties of Graphene. *Nat Nano* **2013**, *8*, 235-246.
15
16
17
18 (91) Ferrari, A. C.; Robertson, J. Resonant Raman Spectroscopy of Disordered, Amorphous, and
19 Diamondlike Carbon. *Phys. Rev. B* **2001**, *64*, 075414.
20
21
22
23 (92) Ferrari, A. C.; Rodil, S. E.; Robertson, J. Interpretation of Infrared and Raman Spectra of
24 Amorphous Carbon Nitrides. *Phys. Rev. B* **2003**, *67*, 155306.
25
26
27
28 (93) Ferrari, A. C. Raman Spectroscopy of Graphene and Graphite: Disorder, Electron-Phonon
29 Coupling, Doping and Nonadiabatic Effects. *Solid State Commun* **2007**, *143*, 47-57.
30
31
32
33 (94) Parvez, K.; Wu, Z.-S.; Li, R.; Liu, X.; Graf, R.; Feng, X.; Müllen, K, Exfoliation of Graphite
34 into Graphene in Aqueous Solutions of Inorganic Salts. *J. Am. Chem. Soc.* **2014** *136*, 6083-
35 6091.
36
37
38
39 (95) Pavlova, A. S.; Obraztsova, E. A.; Belkin, A. V.; Monat, C.; Rojo-Romeo, P.; Obraztsova,
40 E. D. Liquid-Phase Exfoliation of Flaky Graphite. *J. Nanophoton.* **2016**, *10*, 012525.
41
42
43
44 (96) Ummartyotin, S.; Manuspiya, H. A Critical Review on Cellulose: From Fundamental to an
45 Approach on Sensor Technology. *Renew Sust Energ Rev* **2015**, *41*, 402-412.
46
47
48
49 (97) Di Risio, S.; Yan, N. Piezoelectric Ink-Jet Printing of Horseradish Peroxidase: Effect of Ink
50 Viscosity Modifiers on Activity. *Macromol. Rapid Commun.* **2007**, *28*, 1934-1940.
51
52
53
54 (98) Pavinatto, F. J.; Paschoal, C. W. A.; Arias, A. C. Printed and Flexible Biosensor for An-
55 tioxidants Using Interdigitated Ink-jetted Electrodes and Gravure-deposited Active Layer.
56 *Biosens. Bioelectron* **2015**, *67*, 553-559.
57
58
59
60

- 1
2
3
4 (99) Secco, R. A., Kostic, M., deBruyn, J. R. Fluid Viscosity Measurement. In *Measurement, Instrumentation, and Sensors Handbook Spatial, Mechanical, Thermal, and Radiation Measurement*; Webster, J. G., Eren, H. **2014**, CRC Press Taylor & Francis Group.2014; pp 46-1
5
6
7
8
9
10
11 (100) Mezger T. G., **2006** Vincentz Network GmbH & Co KG.
12
13
14 (101) Lin, H.-W.; Chang, C.-P.; Hwu, W.-H.; Ger, M.-D. The Rheological Behaviors of Screen-
15
16
17
18
19 (102) Benchabane, A.; Bekkour, K. Rheological properties of carboxymethyl cellulose (CMC)
20
21
22
23
24 (103) Nijenhuis, K.; McKinley, G. H.; Spiegelberg, S.; Barnes, H. A.; Aksel, N.; Heymann, L. A.;
25
26
27
28
29
30
31
32
33 (104) Irgens, F., *Rheology and Non-Newtonian Fluids*, Springer Verlag, Cham Heidelberg, 2014;
34
35
36
37
38 (105) DeButts, E. H.; Hudy, J. A.; Elliott, J. H. Rheology of Sodium Carboxymethylcellulose
39
40
41
42
43 (106) Elliot, J. H.; Ganz, A. J. Some Rheological Properties of Sodium Carboxymethylcellulose
44
45
46
47
48 (107) Clasen, C.; Kulicke, W.-M. Determination of Viscoelastic and Rheo-optical Material Func-
49
50
51
52
53
54
55 (108) Steffe, J.F. *Rheological Methods in Food Process Engineering*; Freeman Press, 2807 Still
56
57
58
59
60

- 1
2
3
4 (109) Roff, W. J.; Scott, J. R., *Fibres, Films, Plastics and Rubbers, A Handbook of Common*
5 *Polymers Butterworths* 1971.
6
7
8 (110) Xia, W.; Thorpe, M. F. Percolation Properties of Random Ellipses. *Phys. Rev. A.* **1988**, *38*,
9 2650-2656.
10
11
12 (111) Li, W.; Sun, B.; Wu, P. Study on Hydrogen Bonds of Carboxymethyl cellulose Sodium
13 Film with Two-dimensional Correlation Infrared Spectroscopy. *Carbohydr. Polym.* **2009**,
14 *78*, 454-461.
15
16
17 (112) Horvath, A. E.; Lindström, T. The Influence of Colloidal Interactions on Fiber Network
18 Strength. *J Colloid Interface Sci* **2007**, *309*, 511-517.
19
20
21 (113) Dimiev, A. M.; Ceriotti, G.; Metzger, A.; Kim, N. D.; Tour, J. M. Chemical Mass Production
22 of Graphene Nanoplatelets in ~100% Yield. *ACS Nano* **2016**, *10*, 274-279.
23
24
25 (114) Arapov, K.; Rubingh, E.; Abbel, R.; Laven, J.; de With, G.; Friedrich, H. Conductive Screen
26 Printing Inks by Gelation of Graphene Dispersions. *Adv. Funct. Mater.* **2016**, *26*, 586-593.
27
28
29 (115) Roy-Mayhew, J. D.; Bozym, D. J.; Punckt, C.; Aksay, I. A. Functionalized Graphene as a
30 Catalytic Counter Electrode in Dye-Sensitized Solar Cells. *ACS Nano*, **2010**, *4*, 6203-6211.
31
32
33 (116) Audioposter, <http://www.audioposter.com/>
34
35
36 (117) Munson, B. R.; Young, D. F.; Okiishi, T. H.; Huebsch, W. W. *Fundamentals of Fluid Me-*
37 *chanics*, John Wiley & Sons, Inc. 2009.
38
39
40 (118) Rouse, H. *Elementary Mechanics of Fluids*, Dover Publications Inc. New York, 1946.
41
42
43 (119) Holman, J. P. *Heat Transfer*, McGraw-Hill, 1986; pp 210.
44
45
46 (120) Siddiqui, S. W.; Zhao, Y.; Kukukova, A.; Kresta, S. M. Characteristics of a Confined Im-
47 pinging Jet Reactor: Energy Dissipation, Homogeneous and Heterogeneous Reaction Prod-
48 ucts, and Effect of Unequal Flow. *Ind. Eng. Chem. Res.* **2009**, *48*, 7945-7958.
49
50
51
52
53
54
55
56
57
58
59
60

- 1
2
3 (121) Moody, L. F.; Princeton, N. J. Friction Factors for Pipe Flow. *Transactions of the ASME*
4 **1944**, *66*, 671-684.
5
6
7
8 (122) Boxall, J. A.; Koh, C. A.; Sloan, E. D.; Sum, A. K.; Wu, D. T. Droplet Size Scaling of
9 Water-in-Oil Emulsions under Turbulent Flow. *Langmuir* **2012**, *28*, 104-110.
10
11
12 (123) Zhang, J.; Xu, S.; Li, W. High Shear Mixers: A Review of Typical Applications and Stud-
13 dies on Power Draw, Flow Pattern, Energy Dissipation and Transfer Properties. *Chem. Eng.*
14 *Process* **2012**, *57*, 25-41.
15
16
17
18 (124) Kolmogorov, A. N. The Local Structure of Turbulence in Incompressible Viscous Fluids at
19 very Large Reynolds Numbers, *Dokl. Akad. Nauk SSSR* **1941**, *30*, 299-303.
20
21
22 (125) Richardson, L. F. Weather Prediction by Numerical Process. *Cambridge University Press*
23 **1922**, *48*, 282-284.
24
25
26 (126) Varrla, E.; Paton, K. R.; Backes, C.; Harvey, A.; Smith, R. J.; McCauley, J.; Coleman,
27 J. N. Turbulence-assisted Shear Exfoliation of Graphene using Household Detergent and a
28 Kitchen Blender. *Nanoscale* **2014**, *6*, 11810-11819.
29
30
31
32
33
34
35
36
37
38
39
40
41
42
43
44
45
46
47
48
49
50
51
52
53
54
55
56
57
58
59
60